Combinational Post Synthetic Modifications for Single Crystal to Single Crystal Transformations

Sunyoung Shin

Department of Molecular Sciences

Graduate School of UNIST

Combinational Post Synthetic Modifications for Single Crystal to Single Crystal Transformations

A thesis/dissertation
submitted to the Graduate School of UNIST
in partial fulfillment of the
requirements for the degree of
Master of Science

Sunyoung Shin

07/ 08/ 2016
Approved by

Advisor
Myoung-soo Lah

Combinational Post Synthetic Modifications for Single Crystal to Single Crystal Transformations

Sunyoung Shin

This certifies that the thesis/dissertation of Sunyoung Shin is approved.

07/ 08/ 2016

Signature

Advisor: Myoung Soo Lah

Signature

Hoi Ri Moon

Signature

Wonyoung Choe

Abstract

Metal-organic framework, $[Ni_3(btc)_2(bipy)_3(H_2O)_2]\cdot xDMF$ (**1**; btc = benzene-1,3,5-tricarboxylic acid, bipy = 4,4'-bipyridine and DMF = *N,N*-dimethylformamide) was prepared *via de-novo* reaction. $[Ni_3(btc)_2(pz)_3(H_2O)_2]$ (**2**; pz = pyrazine), $[Ni_6(btc)_4(pz)_{4.75}(H_2O)_{5.5}]$ (**3**), *via* two different methods of single crystal transformation which are ligand exchange and heat treatment. By soaking **1** in pz DMF solution, all bipy linkers in **1** were completely exchanged by the shorter pz pillaring linkers to form **2**. Also, the structure of **2** was transformed to **3** by heat treatment.

The single crystal diffraction studies reveal that **1** and **2** are constructed with 2-P sheets linked by bipy and pz, respectively. Dinuclear nickel clusters, $[Ni_2(COO)_2]$ as a secondary building unit (SBU), are doubly linked using two btc ligands to form an 1-periodic (1-P) *noded ribbon* structure. The 1- P *noded ribbons* are further connected *via* mononuclear Ni2 centers to form a corrugated 2-periodic (2-P) sheet of a 3,4-c **bex** topology. The 2-P sheets are pillared *via* bipy or pz linkers to form a 3- periodic (3-P) network. The 3-P networks are considered as a rare 3,4,6-c net of **sqc130** topology consisting of the dinuclear nickel cluster as a 6-c node, the mononuclear Ni ion as a 4-c node, and btc ligand as a 3-c node. The two structures have the same topology, but those structure have a little different relative connectivity.

In transformation process of **3**, the pz linkers of **2** were partially removed by heat treatment, which leaded the rearrangement of coordinated environment of Ni metal. It formed more stable structure at that composition. All single crystal transformations could transform back to original by post-synthetic ligand insertion and exchange.

Contents

Abstract ---------- 4

1. Introduction ---------- 10

2. Experimental Section ---------- 11

2.1. Materials ---------- 11

2.2. General procedures ---------- 11

2.3. Preparation of MOFs ---------- 11

2.4. Reverse transformations of the MOFs *via* post-synthetic ligand insertion and exchange --- 13

2.5. Crystallographic data collection and refinement of the structure ---------- 13

3. Results and Discussion ---------- 19

3.1. *De-novo* synthesis of the MOF and single crystal structure ---------- 19

3.2. Preparation of the isoreticular MOF, 2, by ligand exchange *via* single-crystal to single-crystal transformation ---------- 25

3.3. Preparation of the new MOF, 3, by heat treatment *via* single-crystal to single-crystal transformation ---------- 31

3.4. Transformations of the MOFs ---------- 38

3.5. Sorption behaviors of the MOFs ---------- 40

4. Conclusion ---------- 47

5. Supporting Information ---------- 48

Reference ---------- 52

List of Figures

Figure 1. The crystal structure of **1**: (a) the coordination environments of Ni^{II} and ligands in **1**. (b) the 1-P *noded ribbon* structure. (c) the 2-P sheet structure is formed with 1-P *ribbons* connected by mononuclear Ni2 centers. Top and side view. (d) 3-P structure of **1**. (e) Figures of 6-c node, 4-c node and 3-c node.

Figure 2. The space-filling models of the cage likes pores of **1**.

Figure 3. The alternative view of the network of **1**. The gray, lime and sky-blue balls are 3-c node, 4-c node and 6-c node, respectively.

Figure 4. PXRD patterns for **1**. **1_air-dried** (blue), **I** (**1_MC_air-dried**, dark-cyan)**, II** (**1_ DMF-restored**, pink). **1_air-dried**: **1_as-synthesized** was air-dried for 10 min; **1_MC_air-dried**: **1** presoaked in MC for 3 d was air-dried for 10 min; **1_ DMF-restored**: **1_MC_air-dried** was soaked in DMF for 1 h and then air-dried for 10 min.

Figure 5. ^{1}H NMR spectrum of as-synthesized **1**.

Figure 6. TGA of **1**. As-synthesized **1** and **1** pre-soaked in MC.

Figure 7. The crystal colors of **1,2** and **3**.

Figure 8. ^{1}H NMR spectrum of activated **2a**.

Figure 9. The crystal structure of **2**: (a) the top and side view of 2-P sheet structure of **2**. (b) 3-P structure of **2**.

Figure 10. The space-filling models of the cylindroids likes pores of **2** and accessible aperture dimension of pores; pink : 1.4 Å, yellow : 1.8 Å, and light green : 1.9 Å.

Figure 11. PXRD patterns of as-synthesized **2** and activated **2a**.

Figure 12. TGA trace for **2_MC**.

Figure 13. Coordination mode of mononuclear Ni2 center. The coordinated H_2O molecules are involved in hydrogen bonding interaction with the oxygen atoms from carboxylate groups. The hydrogen bonds are represented in gray dotted lines.

Figure 14. PXRD patterns of heat-treated **2_MC** crystals air-dried at RT heated up to 400 ºC and exposed in the air for an instance before taking the PXRD pattern.

Figure 15. The line graph of pz ratios at heated **2_MC** from ^{1}H NMR spectra. (25, 120, 150, 180, 200, 220, 250, 300, 330 and 360 ºC)

Figure 16. The crystal structure of **3**: (a) the *a*-axis view, (b) the *b*-axis view, (c) *c*-axis view, and (d) 3-P structure of **3**.

Figure 17. The expected transformation process from structure of **2** to structure of **3**.

Figure 18. The detail of connection parts of layers in **2** and **3**. (a),(b) the top view of **2** and **3,** respectively. (c),(d) the *c*-axis view of **2** and **3**, respectively..

Figure 19. The new dinuclear Ni clusters interconnected by a pz linker in **3**, where the dinuclear centers are the statistical average structure of the 25% dinuclear centers and of the 50% mononuclear centers.

Figure 20. (a) The ball-and-stick model and (b) the space-filling model of the cage-like pore **3** with a yellow dummy ball in the center of the cavity.

Figure 21. Scheme of single crystal to single crystal transformations.

Figure 22. PXRD patterns of **1**, **2**, and **3**, and then PXRD patterns of re-transformed **2F3**, **1F2**, and **1F3**.

Figure 23. N_2 sorption behavior (77 K) of **1a**.

Figure 24. CO_2 sorption behavior (195 K) of **1a**.

Figure 25. N_2 sorption behavior (77 K) of **2a** (black), **3** (blue).

Figure 26. CO_2 sorption behavior (195 K) of **2a** (black), **3** (blue).

Figure 27. CO_2 sorption behavior of **1a** (black), **2a** (blue) and **3** (red) at (a) 273 K and (b) 298 K.

Figure 28. Adsorption enthalpy of **1a** (black), **2a** (blue) and **3** (red) by virial theory.

Figure 29. The space-filling models of the **2** and **3** with dummy ball . The largest diameters of pore of **2** and **3** are 1.9 Å and 3.0 Å, respectively.

Figure 30. Pore size distribution of **2a** (green) and **3** (orange).

Figure S1. IR spectrum of **1**.

Figure S2. IR spectrum of **2**.

Figure S3. The crystal color change of 3 in air.

Figure S4. PXRD patterns of **3** by method A and B.

Figure S5. IR spectrum of **3**.

Figure S6. ^{1}H NMR spectra of heated **2_MC**. (25, 120, 150, 180, 200, 220, 250, 300, 330, and 360 ºC)

List of Tables

Table S1. Crystal data and structure refinement for **1**.

Table S2. Crystal data and structure refinement for **2**.

Table S3. Crystal data and structure refinement for **3**.

Nomenclatures

MOF	Metal-Organic Framework
SCSC	Single-crystal to single-crystal
PSM	Post-Synthetic Modification
SBU	Secondary Building Unit
btc	1,3,5-benzenetricarboxylic acid
bipy	4,4'-bipyridine
pz	pyrazine
DMF	*N*,*N*'-Dimethyl Formamide
EA	Elemental Analysis
FT-IR	Fourier Transform-infrared
IR	Infrared
PXRD	Powder X-Ray Diffraction
TGA	Thermogravimetric analysis
NMR	Nuclear Magnetic Resonance
BET	Brauner-Emmett-Teller
N_2	Nitrogen
CO_2	Carbon dioxide
MeOH	Methanol
MC	Methylene Chloride
DCl	Deuterium Chloride
DMSO	Dimethyl Sulfoxide
D_2O	Deuterium Oxide
#	Number
1a	Activated sample of 1
2a	Activated sample of 2
nFm	**n** obtained from **m**

1. Introduction

Metal-organic frameworks (MOFs) is a porous material having various pore size and large surface area generated by the structure of MOFs.[1] In recent decades, MOFs have received huge interest because of their potential applications in gas adsorption and storage,[2] drug delivery,[3] catalysts,[4] and membrane separation.[5] Indeed, new MOFs that are difficult to make in simple synthesis can be easily obtained in high yield through single-crystal to single-crystal transformations.[6] One of the advantages of SCSC transformation is overcoming the limitation of MOF structures by direct synthesis of solvothermal methods which are generally used to prepare MOFs.[6] The driving forces for SCSC transformation vary between physical stimulus[7] and post-synthetic modification (PSM).[8]

Post-synthetic modification is well known as an effective and versatile strategy to improve the physical and chemical properties of the MOFs. PSM can be classified in covalent PSM and Dative PSM; covalent PSM is to give a change in the covalent bond such as functionalization.[8a, 8c] On the other hand, Dative PSM is to give a change in the coordination bond.[8c] The most representative examples of PSM are trans-metalation and ligand exchange.[8b, 8d] Also, Heat-treatment is the normally and conveniently used method among the physical stimulus. Heat-treatment can give various effects in MOFs based on the heat temperature and heat condition, such as transformation, modification, deformation, and etc.[9]

Here in, we present direct synthesis of $[Ni_3(btc)_2(bipy)_3(H_2O)_2]\cdot xDMF$ (**1**; btc = benzene-1,3,5-tricarboxylic acid, bipy = 4,4'-bipyridine and DMF = dimethylformamide), then $[Ni_3(btc)_2(pz)_3(H_2O)_2]$ (**2**; pz = pyrazine) and $[Ni_6(btc)_4(pz)_{4.75}(H_2O)_{5.5}]$ (**3**) *via* two different methods of single crystal transformation which are ligand exchange of PSM and heat treatment of physical stimulus. In these transformation processes, the main structures of SBUs in MOFs are remained as unaltered or slightly changed in the core frame. Therefore, these single crystal transformations could transform back to the original under the remained core frame. We will discuss the structures and properties of **1**, **2**, and **3**.

2. Experimental Section

2.1. Materials

All reagents and solvents were purchased from commercial sources and used without further purification.

2.2. General procedures

Elemental analyses (EA) (C, H, and N) were conducted on an elemental analyzer, Flash 2000, at the Central Research Facilities of the Ulsan National Institute of Science and Technology, Korea. Fourier Transform–infrared (FT–IR) spectra were recorded as KBr pellets with a NICOLET iS 10 FT–IR spectrophotometer (4000–400 cm^{-1}). Powder X-ray diffraction (PXRD) data were recorded using a Bruker D2 Phaser automated diffractometer at room temperature, with a step size of 0.02° in 2θ angle. Simulated PXRD patterns were calculated using the Material Studio program[10] using single-crystal structures. Thermogravimetric analyses (TGA) were performed using Q-600 series from TA instruments at a heating rate of 5 ºC min^{-1} under flowing nitrogen gas. The sample was dried before TGA measurement using flowing N_2 for 30 min. Nuclear magnetic resonance (NMR) spectra were obtained on a 400 MHz FT-NMR spectrometer. All of the gas sorption isotherms were measured using a BELSROP-max (BEL Japan, Inc.) sorption system employing a standard volumetric technique up to saturation pressure. The N_2 (purity of 99.9999 %) sorption isotherms were monitored at 77 K. The adsorption data in the pressure range of < 0.1 P/P_0 were fit to the Brunauer-Emmett-Teller (BET) equation to determine the BET surface area. The CO_2 (purity of 99.9999 %) and CH_4 (purity of 99.995 %) sorption isotherms were measured at 195 K, 273 K, and 298 K, respectively.

2.3. Preparation of MOFs

Preparation of the MOF, $[Ni_3(btc)_2(bipy)_3(H_2O)_2]\cdot x$DMF (1) (where x is a number of DMF molecules in solvent pore per formula unit)), *via de novo* solvothermal reaction. A solid mixture of $Ni(NO_3)_2\cdot 6H_2O$ (0.0850 g, 0.292 mmol), 1,3,5-benzenetricarboxylic acid (H_3btc) (0.0522 g, 0.248 mmol), and 4,4-bipyridine (bipy) (0.0526 g, 0.337 mmol) was dissolved in 48 mL DMF/MeOH (3:1 ratio) mixed solvent of in a 50 mL glass vial. The solution was divided to 5 portions and each aliquot was heated to 120 °C in a flame-sealed glass tube for 7 d to form green cyan crystals. The collected crystals were washed using DMF, and then air-dried at ambient condition for 1 hour. IR spectrum of **1** (KBr, cm^{-1})

(Figure S1): 3392 (vs, b), 3066 (w, b), 2932(m, sh), 1667 (vs), 1634 (s), 1610 (vs), 1558 (s, sh), 1543 (s), 1491 (m), 1433 (s), 1415 (s), 1370 (vs), 1255 (w), 1222 (m), 1101 (m), 1070 (m), 1047 (w), 1012 (w), 939 (w), 860 (w), 817 (m), 770 (m), 729 (m, sh), 718 (m), 662 (w), 636 (m), 573 (w). The activated sample **1a** was prepared by soaking the crystals of **1** in fresh DMF for 3-4 days and in methylene chloride (MC) for additional 2 days, and then vacuum-drying at 50 ºC for overnight. EA was performed using the activated sample re-exposed in air for a couple of minutes before the analysis. EA calc. for $[Ni_3(btc)_2(bipy)_3(H_2O)_2]\cdot 18H_2O$ ($C_{48}H_{60}N_6O_{30}Ni_3$, fw = 1377.10 g/mol). Found (Calc.): C = 41.56 (41.87) %; H = 4.13 (4.39) %; N = 6.56 (6.10).

Preparation of the MOF, $[Ni_3(btc)_2(pz)_3(H_2O)_2]$ (2), *via* post-synthetic ligand exchange of 1. A 50–100 mg amount of the crystals of **1** soaked in DMF was transferred into a 10 mL amount of 0.5 M pz DMF solution in a 20 mL vial and the vial was kept in an oven at 100 °C for 1-2 weeks depending on the sample amount. The solution was refreshed 2–3 times during the soaking. The progress of the ligand exchange was monitored by using PXRD. When the ligand exchange was completed, the cyan green crystals were harvested and washed more than three times using fresh DMF, and then air-dried at ambient temperature for an hour. IR spectrum of **2** (KBr, cm^{-1}) (Figure S2): 3380 (vs, b), 3116 (m), 3068 (m), 2956 (w), 2932 (w), 2850 (w), 1679 (vs), 1640 (vs), 1611 (m), 1555 (m), 1534 (s), 1487 (w), 1464 (w), 1436 (m), 1418 (m, sh), 1385 (m), 1373 (m), 1257 (w), 1218 (vw), 1162 (w), 1115 (w), 1098 (m), 1062 (m), 1032 (vw), 980 (vw), 941 (w), 819 (m), 769 (s), 733 (s), 718 (s), 662 (m), 571 (w), 524 (w), 482 (m), 453 (w), 430 (vw). The activated sample **2a** was prepared by soaking the crystals of **2** in fresh DMF for 3-4 days and in MC for additional 2 days, and then vacuum-drying at room temperature for a day. EA was performed using the sample of **2a** re-exposed in air for several minutes before the analysis. EA calc. for $[Ni_3(btc)_2(pz)_3(H_2O)_2]\cdot 15H_2O$ ($C_{30}H_{42}N_6O_{27}Ni_3$, fw = 1094.76 g/mol). Found (Calc.): C = 32.89 (32.91) %; H = 3.45 (3.87) %; N = 7.75 (7.68) %.

Preparation of the MOF, $[Ni_6(btc)_4(pz)_{4.75}(H_2O)_6]\cdot 12H_2O$ (3), *via* heat treatment of 2. Method A. When the pale bluish green crystals of **2** (50–100 mg) was heated up to 200 ºC in 10 ºC/min heating rate, kept for an hour, and cooled down to ambient temperature under flowing N_2, the crystals turned dark orange. The light green crystals of **3** was obtained exposing the dark orange crystals in air (Figure S3). Method B. **3** can be alternatively prepared by vacuum-drying **2**, presoaked for two days in MC, at 200 ºC for 1 h and then exposing in air for 2-3 minutes. PXRD patterns of **3** obtained by both method A and method B are not distinguishable to each other (Figure S4). IR of **3** (KBr, cm^{-1}) (Figure S5): 3354 (vs, b), 3120 (m), 3072 (m), 1683 (w), 1652 (m), 1634 (vs), 1621 (m), 1615 (m),1574 (w), 1568 (w), 1558 (s), 1538 (m), 1532 (w), 1506 (w), 1435 (s), 1423 (m), 1373 (vs), 1162 (w), 1120 (m), 1088 (vw), 1064 (m), 939 (vw), 817 (vw), 769 (s), 733 (s), 719 (m), 560 (w), 483 (m), 451 (w), 440 (vw). EA calc. for **3**,

$[Ni_6(btc)_4(pz)_{4.75}(H_2O)_6]\cdot 18H_2O$ ($C_{55}H_{67}N_{9.5}O_{48}Ni_6$, fw = 1981.31 g/mol). Found (Calc.): C = 33.34 (31.82) %; H = 3.41 (3.25) %; N = 6.72 (6.96) %.

2.4. Reverse transformations of the MOFs *via* post-synthetic ligand insertion and exchange

Reverse transformation of 3 to 2 *via* post-synthetic ligand insertion. A 50–100 mg amount of **3** crystals was soaked in a 10 mL 0.5 M pz DMF solution in a 20 mL vial and was kept in at ambient condition for 3-5 days depending on the sample amount. When the transformation process was completed, the crystals were washed several times using fresh DMF, and then air-dried for 1 hr.

Reverse transformation of 2 to 1 *via* post-synthetic ligand exchange. A 50–100 mg amount of **2** crystals was immersed to a 10 mL 0.5 M bipy DMF solution in a vial and kept at 100 °C for 1-2 weeks depending on the sample amount. The solution was exchanged 2–3 times during the soaking and the progress of the ligand exchange was monitored by PXRD. When the ligand exchange was completed, the crystals were harvested and washed using fresh DMF more than three times, and then air-dried at ambient temperature for an hour.

Transformation of 3 to 1 *via* post-synthetic ligand insertion and exchange. A 50–100 mg amount of **3** crystals was soaked in a 10 mL 0.5 M bipy DMF solution in a vial and kept at 100 °C for 1-2 weeks depending on the sample amount. The solution was exchanged 2–3 times during the soaking. When the process of transformation was completed, the crystals were harvested and washed using fresh DMF several times, and then air-dried at ambient condition for an hour.

2.5. Crystallographic data collection and refinement of the structure

Crystals of **1, 2**, and **3** were coated with paratone-*N* oil and the diffraction data were measured at 100 K with synchrotron radiation (λ = 0.66999 Å, 0.70000 Å, and 0.63000 Å, respectively) on an ADSC Quantum-210 detector at 2D SMC with a silicon (111) double crystal monochromator (DCM) at the Pohang Accelerator Laboratory, Korea. The ADSC Q210 ADX program[11] was used for data collection and HKL3000sm (Ver. 703r)[12] was used for cell refinement, reduction and absorption correction. The structures were solved by direct method and refined by full-matrix least-squares calculation with the SHELX software package.[13]

1. One and half nickel atoms (one nickel atom is at general position and the other half nickel atom is on a crystallographic 2-fold symmetry axis), one btc ligand, one and half disordered bipy linkers (one

bipy linker is at general position and the other half bipy linker is on a crystallographic 2-fold symmetry axis) and one ligated water molecule are observed as an asymmetric unit. All non-hydrogen atoms are refined anisotropically; All non-hydrogen atoms are refined anisotropically; the hydrogen atoms were assigned isotropic displacement coefficients U(H) = 1.2U (C) and their coordinates were allowed to ride on their respective atoms. The least-squares refinement of the structural model was performed under displacement parameter restraints such as DANG, DFIX, FLAT, ISOR and SIMU for disordered bipy molecules. The final refinement was performed with the modification of the structure factors for the electron densities of the disordered solvents (1670 $Å^3$, 44.2% of the total unit cell volume; 444 electrons equivalent to the electrons of ~11 DMF molecules or of 24.5 methanol molecules or of their combination per unit cell) using the SQUEEZE option of PLATON. [14] Refinement converged at a final $R1$ = 0.0581 and $wR2$ = 0.1670 for 5902 reflections with $I > 2\sigma(I)$; $R1$ = 0.0829 and $wR2$ = 0.1759 for all 9271 reflections. The largest difference peak and hole were 0.876 and –0.629 $e \cdot Å^{-3}$, respectively.

2. One and half nickel atoms (one nickel atom is at general position and the other half nickel atom is on a crystallographic 2-fold symmetry axis), one btc ligand, one and half pz linkers (one pz linker is at general position and the other half pz linker is on a crystallographic 2-fold symmetry axis) and one ligated water molecule are observed as an asymmetric unit. All non-hydrogen atoms are refined anisotropically; the hydrogen atoms were assigned isotropic displacement coefficients U(H) = 1.2U (C) and 1.5U (O_{water}), and their coordinates were allowed to ride on their respective atoms except for water. The final refinement was performed with the modification of the structure factors for the electron densities of the disordered solvents (1126.8 $Å^3$, 45.4% of the total unit cell volume; 308 electrons equivalent to the electrons of ~7.7 DMF molecules per unit cell) using the SQUEEZE option of PLATON.[S4] Refinement converged at a final $R1$ = 0.0962 and $wR2$ = 0.2715 for 2707 reflections with $I > 2\sigma(I)$; $R1$ = 0.1243 and $wR2$ = 0.2975 for all 4044 reflections. The largest difference peak and hole were 1.131 and –0.903 $e \cdot Å^{-3}$, respectively.

3. Six nickel atoms at ten crystallographically different sites (four nickel atoms are at general positions, one nickel atom is at two crystallographically independent general positions of total of single site occupancy, and the remaining one nickel atom is at four crystallographically independent positions on two different *m* symmetry planes of total of single site occupancy), four btc ligands, four and three half pz linkers at nine crystallographically different sites (two pz linkers are at general positions, two pz linkers are at four different sites on a crystallographic *m* symmetry plane, 0.375 pz linker is on two crystallographic different 2/*m* symmetry sites and 0.375 pz linker is on a crystallographic 2-fold symmetry axis) and five and half ligated water molecules at ten crystallographically different sites are observed as an asymmetric unit. All non-hydrogen atoms are refined anisotropically; the hydrogen atoms

were assigned isotropic displacement coefficients U(H) = 1.2U (C) and their coordinates were allowed to ride on their respective atoms. The least-squares refinement of the structural model was performed under displacement parameter restraints such as DANG, DFIX and ISOR. The final refinement was performed with the modification of the structure factors for the electron densities of the disordered solvents (4810.8 $Å^3$, 29.0% of the total unit cell volume; 990 electrons equivalent to the electrons of ~50 water molecules per unit cell) using the SQUEEZE option of PLATON.[S4] Refinement converged at a final $R1$ = 0.1423 and $wR2$ = 0.3795 for 5044 reflections with $I > 2\sigma(I)$; $R1$ = 0.2611 and $wR2$ = 0.4281 for all 16571 reflections. The largest difference peak and hole were 1.489 and −1.080 $e \cdot Å^{-3}$, respectively.

A summary of the crystal and some crystallography data is given in Tables S1-S3. CCDC 1492769, 1492770, and 1492771 contain the supplementary crystallographic data for this paper. The data can be obtained free of charge at www.ccdc.cam.ac.uk/conts/retrieving.html or from the Cambridge Crystallographic Data Centre, 12, Union Road, Cambridge CB2 1EZ, UK.

Table S1. Crystal data and structure refinement for **1**.

Empirical formula	$C_{48}H_{34}N_6Ni_3O_{14}$	
Formula weight	1094.94	
Temperature	100(2) K	
Wavelength	0.66999 Å	
Crystal system	Monoclinic	
Space group	*P*2/*c*	
Unit cell dimensions	a = 18.618(4) Å	α = 90°
	b = 11.259(2) Å	β = 114.96(3)°
	c = 19.860(4) Å	γ = 90°
Volume	3774.4(13) $Å^3$	
Z	2	
Density (calculated)	0.963 Mg/m^3	
Absorption coefficient	0.636 mm^{-1}	
F(000)	1120	
Crystal size	0.10 x 0.08 x 0.02 mm^3	
Theta range for data collection	1.14 to 26.46°.	
Index ranges	–24<=h<=24, –14<=k<=14, –26<=l<=26	
Reflections collected	33545	
Independent reflections	9271 [R(int) = 0.0658]	
Completeness to theta = 26.46°	99.8 %	
Absorption correction	Semi-empirical from equivalents	
Max. and min. transmission	0.9874 and 0.9391	
Refinement method	Full-matrix least-squares on F^2	
Data / restraints / parameters	9271 / 58 / 398	
Goodness-of-fit on F^2	0.962	
Final R indices [I>2sigma(I)]	R1 = 0.0581, wR2 = 0.1670	
R indices (all data)	R1 = 0.0829, wR2 = 0.1759	
Extinction coefficient	0.0103(10)	
Largest diff. peak and hole	0.876 and –0.629 $e \cdot Å^{-3}$	

Table S2. Crystal data and structure refinement for **2**.

Empirical formula	$C_{30}H_{22}N_6O_{14}Ni_3$	
Formula weight	866.66	
Temperature	100(2) K	
Wavelength	0.700 Å	
Crystal system	Monoclinic	
Space group	*P*2/*c*	
Unit cell dimensions	a = 20.395(4) Å	α = 90°
	b = 6.9410(14) Å	β = 119.18(3)°
	c = 20.070(4) Å	γ = 90°
Volume	2480.5(11) $Å^3$	
Z	2	
Density (calculated)	1.160 Mg/m^3	
Absorption coefficient	1.129 mm^{-1}	
F(000)	880	
Crystal size	0.08 x 0.03 x 0.02 mm^3	
Theta range for data collection	2.253 to 23.997°.	
Index ranges	–23<=h<=23, –8<=k<=8, –23<=l<=23	
Reflections collected	13992	
Independent reflections	4044 [R(int) = 0.0781]	
Completeness to theta = 23.997°	99.5 %	
Absorption correction	Semi-empirical from equivalents	
Max. and min. transmission	0.978 and 0.915	
Refinement method	Full-matrix least-squares on F^2	
Data / restraints / parameters	4044 / 0 / 247	
Goodness-of-fit on F^2	1.040	
Final R indices [I>2sigma(I)]	R1 = 0.0962, wR2 = 0.2715	
R indices (all data)	R1 = 0.1243, wR2 = 0.2975	
Largest diff. peak and hole	1.131 and –0.903 $e \cdot Å^{-3}$	

Table S3. Crystal data and structure refinement for **3**.

Empirical formula	$C_{110}H_{84}N_{19}O_{59}Ni_{12}$	
Formula weight	3320.48	
Temperature	100(2) K	
Wavelength	0.630 Å	
Crystal system	Monoclinic	
Space group	*C*2/*m*	
Unit cell dimensions	a = 32.243(6) Å	α = 90°
	b = 27.320(6) Å	β = 109.31(3)°
	c = 19.956(4) Å	γ = 90°
Volume	16590(6) $Å^3$	
Z	4	
Density (calculated)	1.329 Mg/m^3	
Absorption coefficient	1.011 mm^{-1}	
F(000)	6740	
Crystal size	0.08 x 0.02 x 0.02 mm^3	
Theta range for data collection	2.196 to 22.998°.	
Index ranges	–39<=h<=39, –33<=k<=33, –24<=l<=24	
Reflections collected	54894	
Independent reflections	16571 [R(int) = 0.1169]	
Completeness to theta = 22.210°	98.0 %	
Absorption correction	Semi-empirical from equivalents	
Max. and min. transmission	0.980 and 0.923	
Refinement method	Full-matrix least-squares on F^2	
Data / restraints / parameters	16571 / 143 / 979	
Goodness-of-fit on F^2	1.077	
Final R indices [I>2sigma(I)]	R1 = 0.1423, wR2 = 0.3759	
R indices (all data)	R1 = 0.2611, wR2 = 0.4281	
Largest diff. peak and hole	1.489 and –1.080 $e \cdot Å^{-3}$	

3. Results and Discussion

3.1. *De-novo* synthesis of the MOF and single crystal structure

A microporous 3-P MOF with mixed ligands was obtained by a simple one-pot reaction. The solvothermal reaction of $Ni(NO_3)_2 \cdot 6H_2O$ as a source for potential metal-based nodes with the two different types of ligands, btc as an anionic tritopic node and bipy as a neutral ditopic linker, in DMF/MeOH at 120 °C for 7 d led to the formation of green cyan crystals, $[Ni_3(btc)_2(bipy)_3(H_2O)_2]$ (**1**). Single-crystal X-ray structural analysis revealed that **1** crystallizes in the monoclinic space group *P*2/*c*. As shown in Figure 1a, two N^{II} ions (Ni1 and Ni2) in two different coordination environments adopt the same *trans*-$[N_2O_4]$ octahedral geometry. For Ni1, the equatorial plane of the octahedron is defined by four oxygen atoms from three carboxylates of btc ligands and the axial positions are occupied by two nitrogen atoms from bipy ligands. Ni2 is ligated by two monodentate carboxylates, two nitrogen atoms from bipy ligands and two water molecules. Ni1 is bridged *via* carboxylates in a bis(*syn-syn*) binding mode to form a dinuclear nickel cluster, $[Ni_2(COO)_2]$, as a secondary building unit (SBU), and the SBUs are doubly linked using two btc ligands to form a 1-P *noded ribbon* structure (Figure 1b). The 1-P *noded ribbons* are further connected *via* mononuclear Ni2 centers to form a corrugated 2-P sheet of a 3,4-c **bex** topology (Figure 1c).[*] The 2-P sheets are pillared *via* bipy linkers to form a 3-P network (Figure 1d), where two different types of bipy pillaring are observed. The first type of the pillaring is through the dinuclear nickel clusters. The dinuclear nickel ions (Ni1 ions) of the SBU are doubly connected to the dinuclear nickel ions of the adjacent 2-P sheets. The second type of the pillaring is through the nickel ion (Ni2) that interconnects the 1-P *noded ribbons* to the 2-P sheet. The 3-P network is a rare 3,4,6-c net of **sqc130** topology consisting of btc ligand as a 3-c node, the mononuclear Ni ion as a 4-c node and the dinuclear nickel cluster as a 6-c node (Figure 1e). The pores of **1** are cage-like pores having 2.9 Å and 3.0 Å dimension, respectively. (Figure 2).

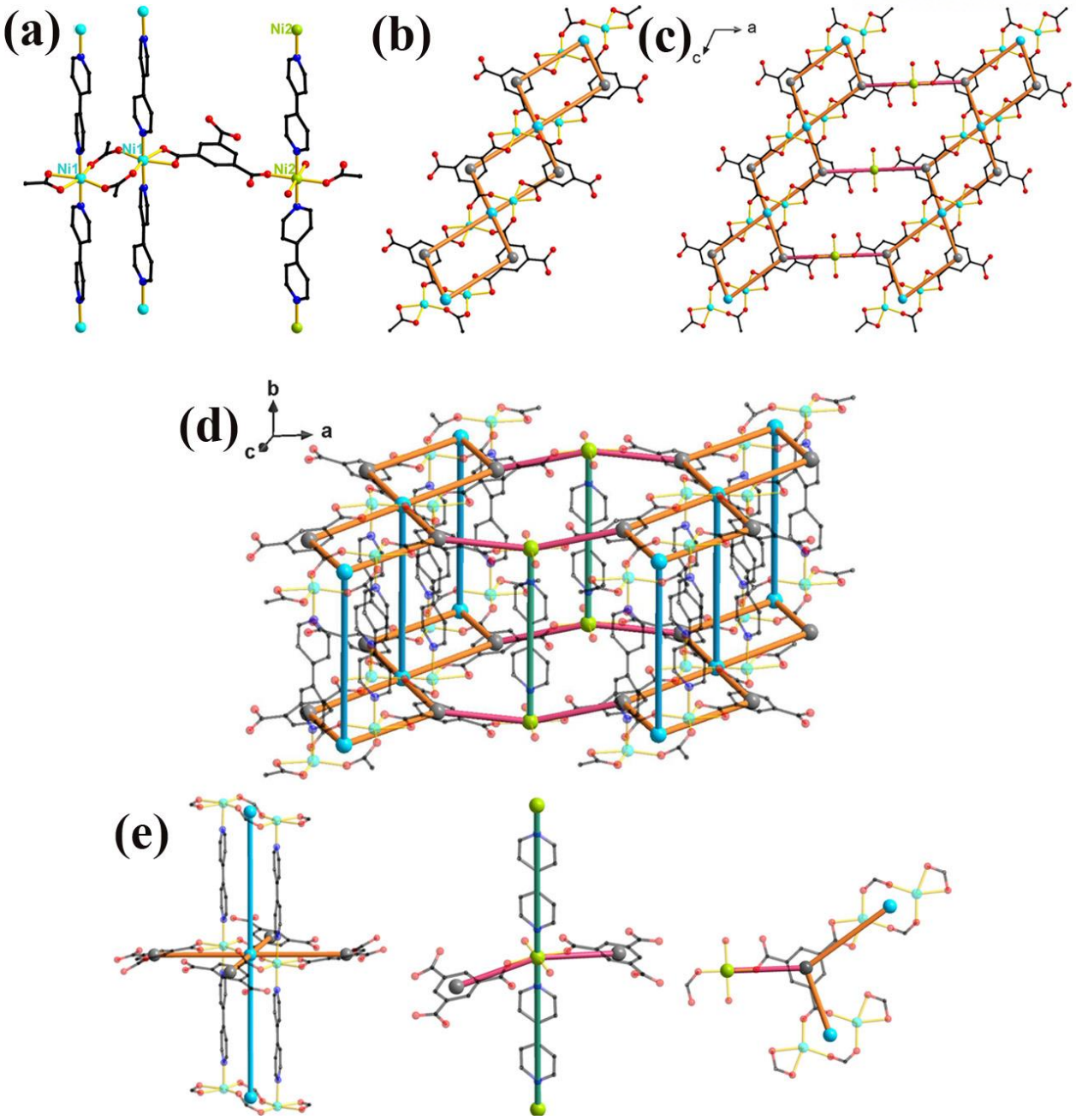

Figure 1. The crystal structure of **1**: (a) the coordination environments of Ni^{II} and ligands in **1**. (b) the 1-P *noded ribbon* structure. (c) the 2-P sheet structure is formed with 1-P *ribbons* connected by mononuclear Ni2 centers. Top and side view. (d) 3-P structure of **1**. (e) Figures of 6-c node, 4-c node and 3-c node.

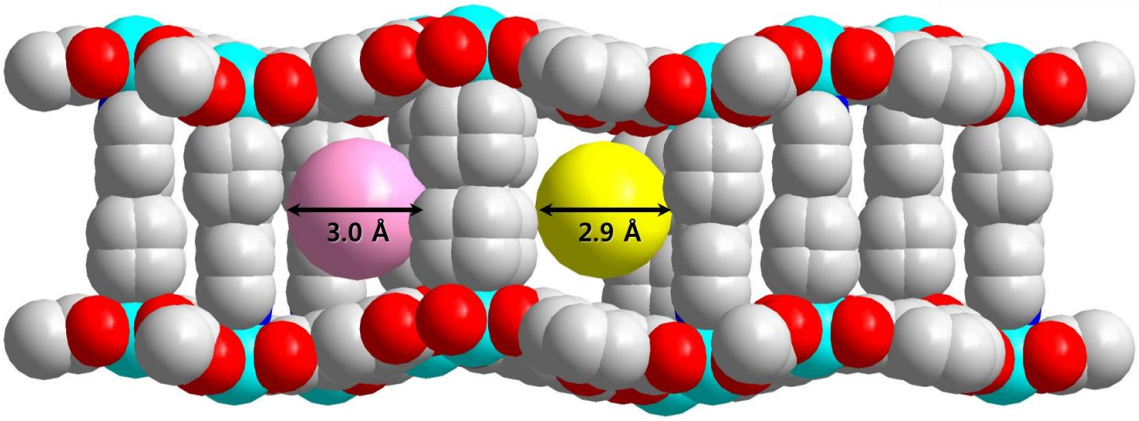

Figure 2. The space-filling models of the cage likes pores of **1**.

1 could be alternatively viewed as a 3-P network generated from the 2-P layers interconnected by the 1-P chains, where the 2-P layers are from the 1-P noded ribbons doubly linked by using ditopic bipy linkers and the 1-P chains are from the mononuclear Ni ion singly linked by using the same bipy linkers (Figure 3).

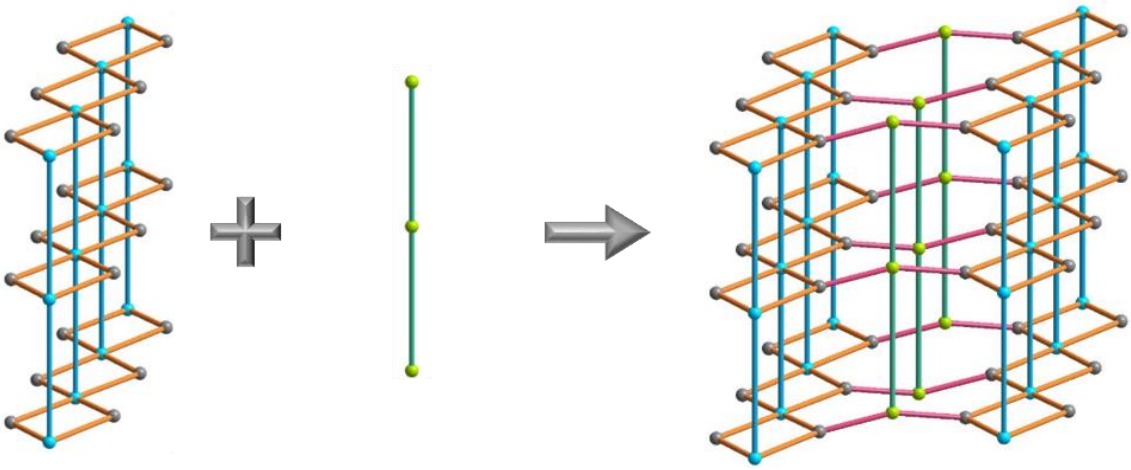

Figure 3. The alternative view of the network of **1**. The gray, lime and sky-blue balls are 3-c node, 4-c node and 6-c node, respectively.

The bulk purity of the sample was confirmed from the comparison of the observed PXRD pattern of as-synthesized **1** and the simulated PXRD pattern of the single-crystal structure model of **1** (Figure 4). The observed pattern of as-synthesized **1** matches well with the simulated pattern. However, the PXRD

pattern of **1** exposed at ambient condition approximately for 10 min is similar to but not the same as the simulated pattern. Even a small amount of the guest solvent loss in the pore leads to a slight distortion of the framework. The sample, presoaked in MC and exposed ambient condition approximately for 10 min, showed significant loss of crystallinity. The solvent loss results in the collapse of the framework. However, the collapsed framework could be restored simply soaking the collapsed sample in DMF. The PXRD pattern of the restored sample is the same as that of **1** exposed at ambient condition. The ^{1}H nuclear magnetic resonance (NMR) spectrum of as-synthesized **1** digested in DCl/d_6-DMSO solution also indicates that the ratio of btc ligands and bipy linkers in the bulk sample is the same as that in the single crystal structure (Figure 5).

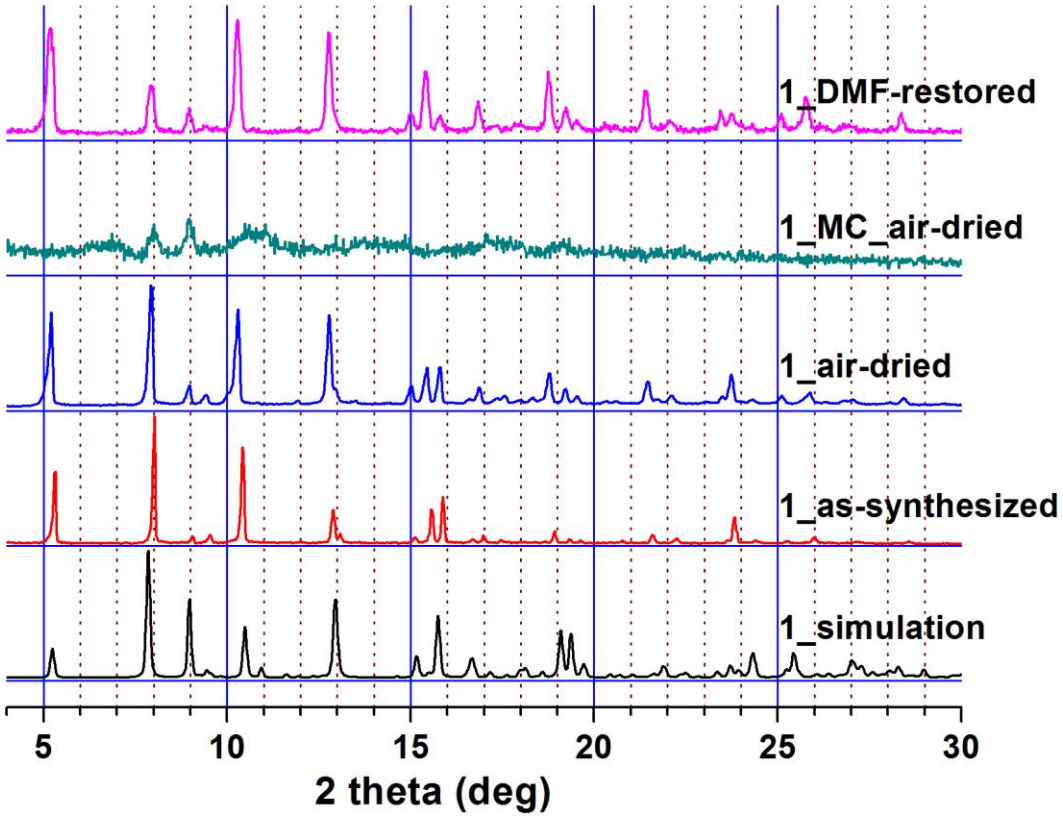

Figure 4. PXRD patterns for **1**. **1_air-dried** (blue), **I** (**1_MC_air-dried**, dark-cyan)**, II** (**1_DMF-restored**, pink).**1_air-dried**: **1_as-synthesized** was air-dried for 10 min; **1_MC_air-dried**: **1** presoaked in MC for 3 d was air-dried for 10 min; **1_ DMF-restored**: **1_MC_air-dried** was soaked in DMF for 1 h and then air-dried for 10 min.

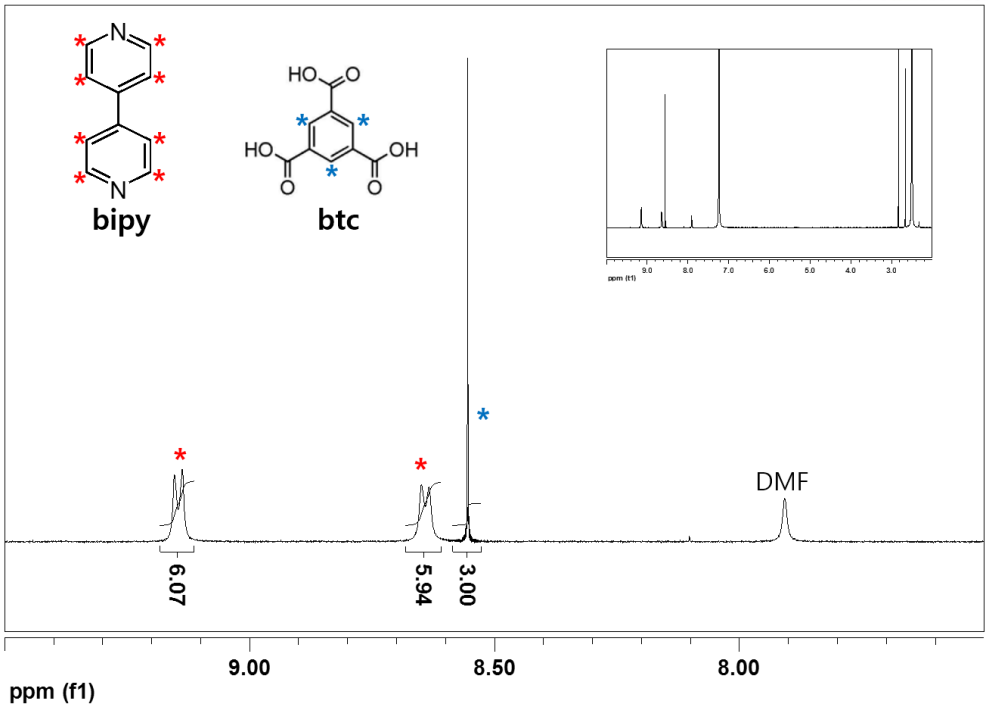

Figure 5. ^{1}H NMR spectrum of as-synthesized **1**.

TGA were performed using two different states of the sample **1**. One is as-synthesized **1** exposed at ambient condition for an hour. The other is **1** presoaked in MC and then exposed at ambient condition for an hour. As-synthesize **1** showed at least three-step weight losses (Figure 6). The first 6.9 wt% loss up to 70 °C corresponds to the loss of 6 water molecules (calc. 6.8 wt%) in the pore adsorbed in air. The second 24.7 wt% loss up to 250 °C corresponds to the loss of 5.5 DMF molecules (calc. 25.3 wt%). The sample starts to decompose at ~ 320 °C. The sample **1** presoaked in MC showed two-step weight losses. The first 10.2 wt% loss up to 250 °C corresponds to the weight loss of 1.5 MC molecules (calc. 10.5 wt%) in the pore and then starts to decompose approximately at the same temperature, ~ 320 °C.

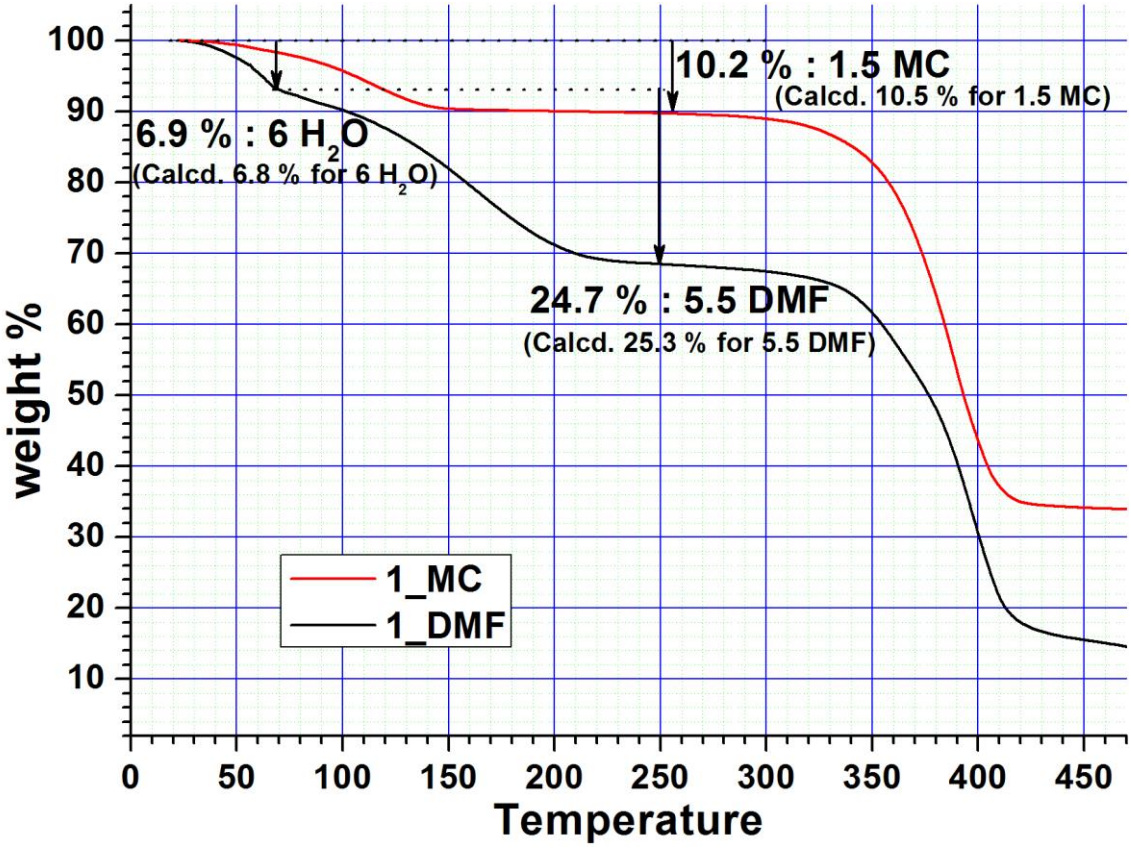

Figure 6. TGA of **1**. As-synthesized **1** and **1** pre-soaked in MC.

3.2. Preparation of the isoreticular MOF, 2, by ligand exchange *via* single-crystal-to-single-crystal transformation

Preparation of the isoreticular MOF, 2. The 3-P MOF with bipy pillar, $[Ni_3(btc)_2(bipy)_3(H_2O)_2]$ (**1**), could be transformed to another isoreticular MOF with pz pillar, $[Ni_3(btc)_2(pz)_3(H_2O)_2]$ (**2**), by pillar exchange. Simple soaking **1** in a pz DMF solution at 100 ºC led to pillar exchange. Green cyan crystals of **1** turned to cyan green crystals of **2** (Figure 7). The complete exchange of the pillaring ligand was confirmed by ^{1}H NMR spectroscopy. The ^{1}H NMR spectrum of activated **2a** digested in DCl/D_2O solution showed that bipy pillar was completely removed and btc ligand and pz pillar are present in the stoichiometric ratio (Figure 8).

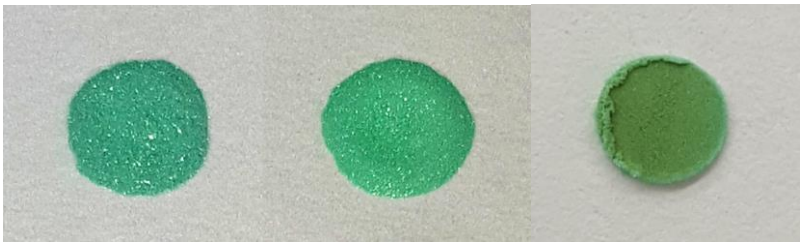

Figure 7. The crystal colors of **1**, **2** and **3**.

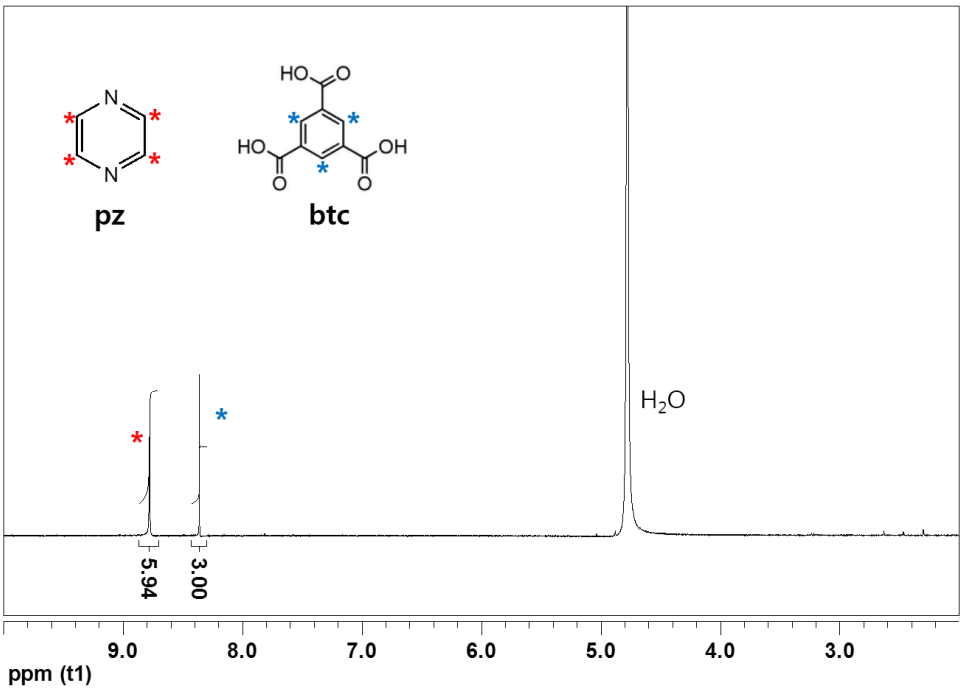

Figure 8. ^{1}H NMR spectrum of activated **2a**.

Single crystal structure of 2. Though the space group of **2**, *P*2/*c*, is the same as that of **1**, the lattice parameters of **2** (a = 20.395(4) Å, b = 6.9410(14) Å, c = 20.070(4) Å, β = 119.18(3)°) are significantly different from those of **1** (a = 18.618(4) Å, b = 11.259(2) Å, c = 19.860(4) Å, β = 114.96(3)°). The replacement of bipy, aligned along the crystallographic *b*-axis in **1**, to pz led to a significant reduction of the *b*-axis distance in **2** from ~ 11 Å to ~ 7 Å. Noticeable differences are also observed in the β angles together with in the *a*- and the *c*-axis distances, which implies the pillar exchange accompanies the distortion of the 2-P sheet structure of the **bex** net topology (Figure 1c). The single crystal structure analysis of **2** confirmed the complete replacement of the pillaring ligands. Even though the net topology of **2** is the same as that of **1**, the connectivity of **2** is not the same as that of **1** (Figure 9). In addition to the pillaring ligand replacement, the interconnection between the 1-P noded ribbons in the 2-P sheet was changed too. The relative interconnection between the 1-P *ribbons* in **2** is different from that in **1**. The linkages between carboxylate pairs (dashed pale pink stick), *via* mononuclear Ni2 centers interconnecting the adjacent 1-P *ribbons* to form the 2-P sheet, has shifted to the linkages of the other carboxylate pairs (solid purple stick) (Figure 9a), which leads to slight distortion of the 2-P sheet structure in the crystallographic *ac*-plane. The pores of **2** are cylindroid-like pores having small accessible aperture dimensions (1.4 Å, 1.8 Å, and 1.9 Å) and they are intercrossing each other (Figure 10).

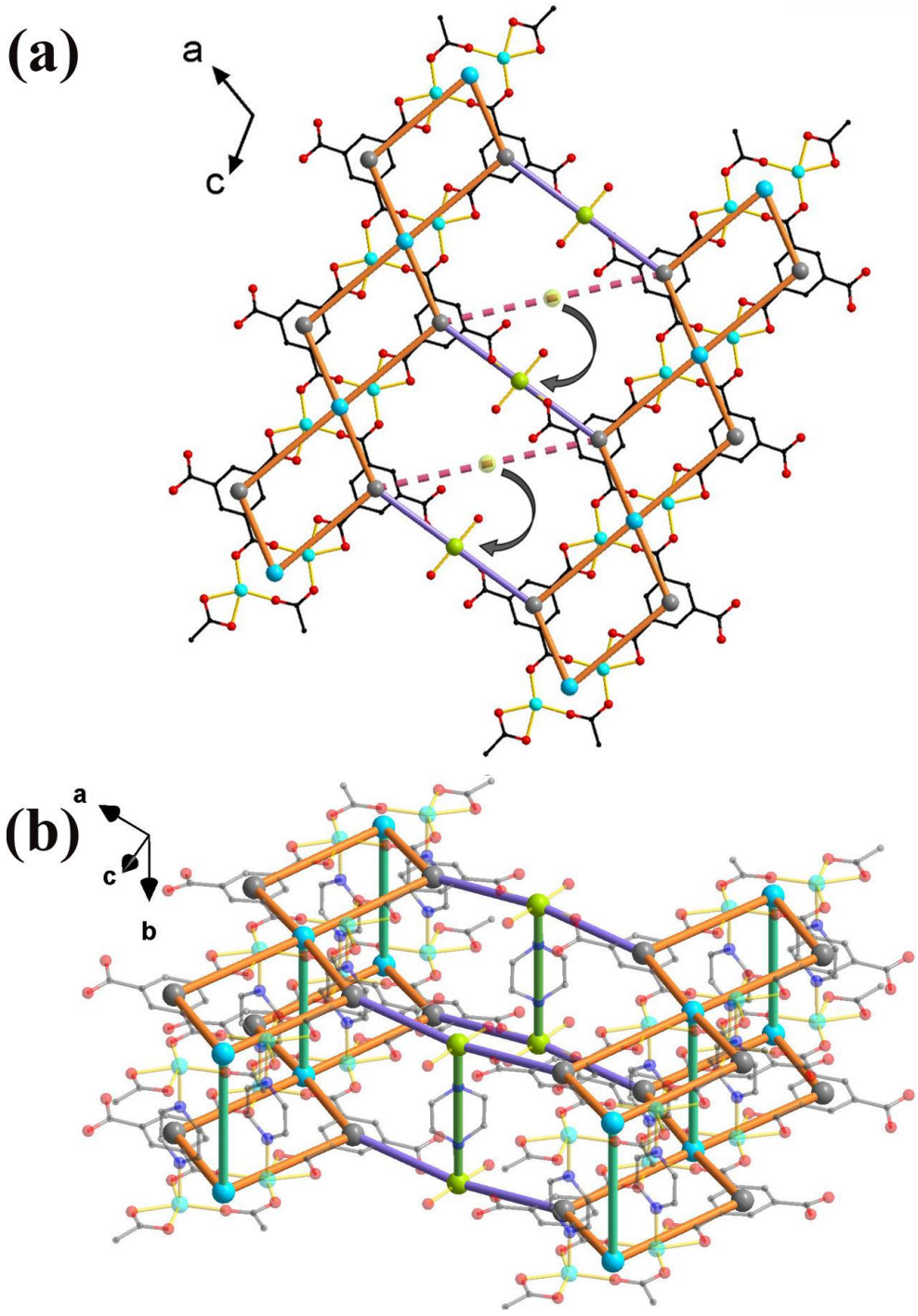

Figure 9. The crystal structure of **2**: (a) the top and side view of 2-P sheet structure of **2**. (b) 3-P structure of **2**.

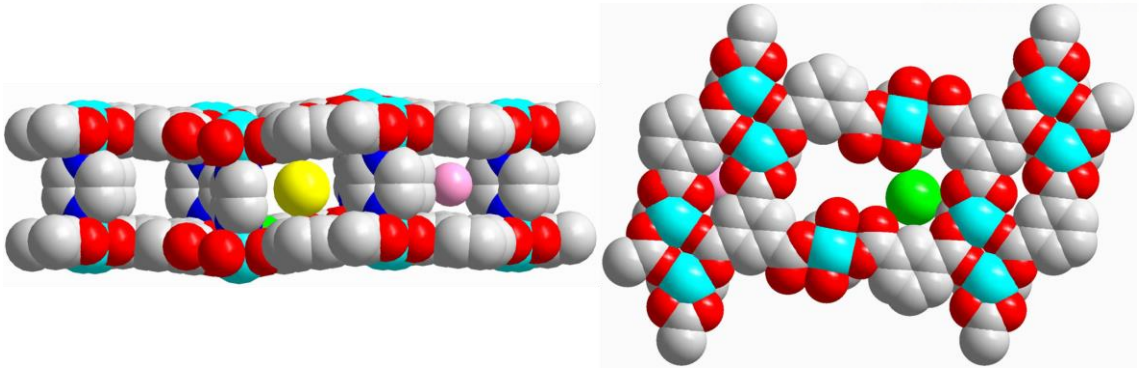

Figure 10. The space-filling models of the cylindroids likes pores of **2** and accessible aperture dimension of pores; pink : 1.4 Å, yellow : 1.8 Å, and light green : 1.9 Å.

Bulk identity and stability of 2. The bulk purity of **2** was also checked by the comparison of the observed and simulated PXRD patterns (Figure 11). The observed PXRD pattern of as-synthesized **2** matches well with the simulated pattern from the single crystal structure model. Contrary to **1**, even activated **2a** is still crystalline and its PXRD pattern is very similar to that of as-synthesized **2**. The slight shifts of the most peaks to higher diffraction angles indicate that the structure is quite rigid but there is a little bit of shrinkage of the overall framework structure when the solvent molecules are removed from the pore.

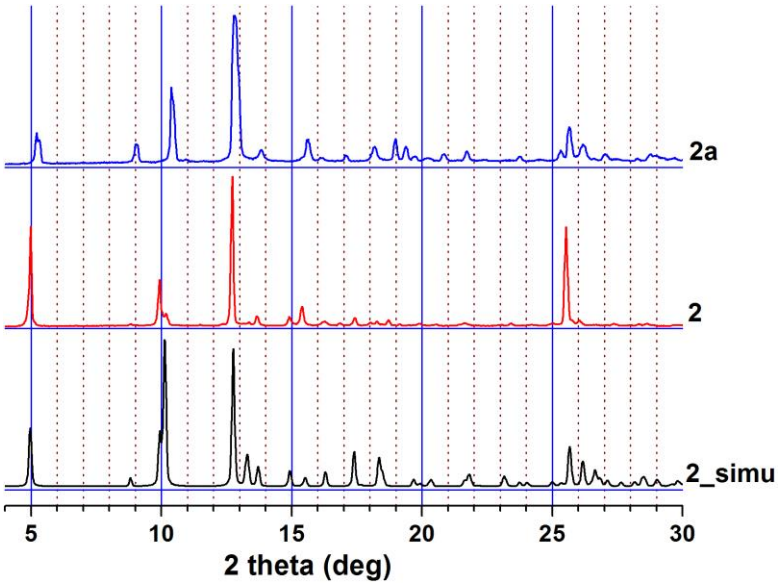

Figure 11. PXRD patterns of as-synthesized **2** and activated **2a.**

Thermal properties of 2. The thermal properties of **2** was evaluated using TGA. The analysis was done using **2** presoaked in MC (**2_MC**). The TGA profile indicates at least six-step weight losses (Figure 12). The first two-step weight loss up to 150 ºC (15.2 wt%) corresponds to the loss of 1.5 MC molecules (calcd. 12.7 wt%) and 1.5 H_2O molecules (calcd. 2.5 wt%) in the pore. The next two-step weight loss from 150 ºC to 380 ºC corresponds to some pz pillars and the ligated water molecules. The weight loss from 150 ºC to 270 ºC (4.5 wt%) is the loss of 0.6 pz pillar (calcd. 4.7 wt%) and that from 270 ºC to 380 ºC (17.7 wt%) is the loss of two water molecules (calcd. 4.7 wt%). The amount of the pz pillar lost during the heating process up to 270 ºC was confirmed by using the ^1H NMR spectrum of the sample prepared by the same manner used for the TGA heating process. Even though the boiling point of pz is higher than that of water, the loss of some pz linkers prior to that of the ligated H_2O molecules is due to the intramolecular hydrogen-bond interaction of the ligated water molecules with the carboxylate oxygens of the btc ligands (Figure 13). The weight loss from 270 ºC to 300 ºC (17.7 wt%) matches with the loss of two coordinated H_2O molecules (calcd. 3.5 wt%) and 1.8 pz pillars (calcd. 14.2 wt%). The final two-step weight loss starts at 380 ºC corresponds to the thermal decomposition of the remaining structure together with the loss of the remaining 0.6 pz pillar.

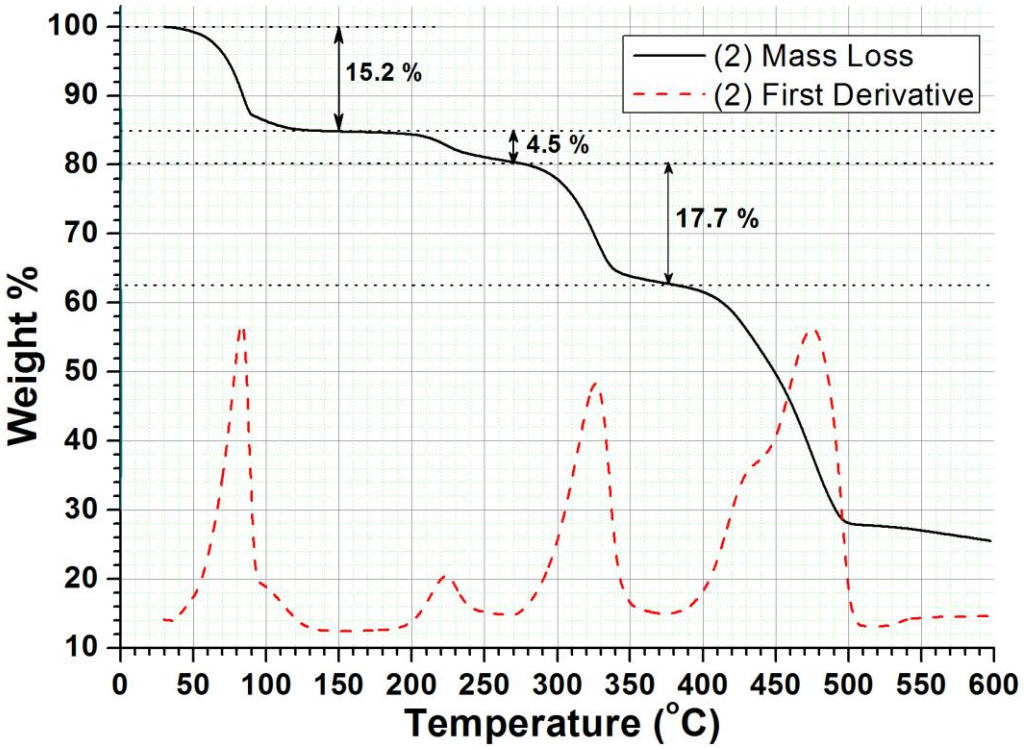

Figure 12. TGA trace for **2_MC**.

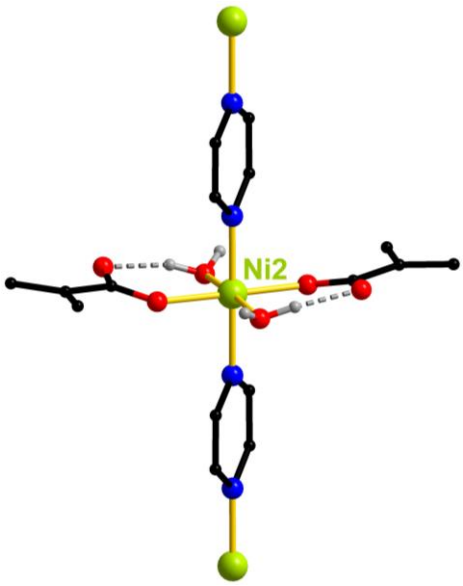

Figure 13. Coordination mode of mononuclear Ni2 center. The coordinated H_2O molecules are involved in hydrogen bonding interaction with the oxygen atoms from carboxylate groups. The hydrogen bonds are represented in gray dotted lines.

3.3. Preparation of the new MOF, 3, by heat treatment *via* single-crystal to single-crystal transformation

PXRD patterns of heat-treated 2. The heat-treated samples were prepared using **2** crystals presoaked in MC. The crystals were heated up to a given temperature in 10 ºC min^{-1} increase rate and kept for 1 hr. After cooling down to ambient temperature under flowing nitrogen, the crystals were exposed in air before PXRD measurement. The PXRD patterns showed that **2** is stable up to 150 ºC. A set of new diffraction peaks was appeared at 180 ºC together with the diffraction peaks from **2**. The diffraction peaks corresponding to **2** were completely disappeared at 200 ºC and only the set of new diffraction peaks was observed. The new crystalline phase is stable at 220 ºC but starts to lose its crystallinity at the higher temperatures.

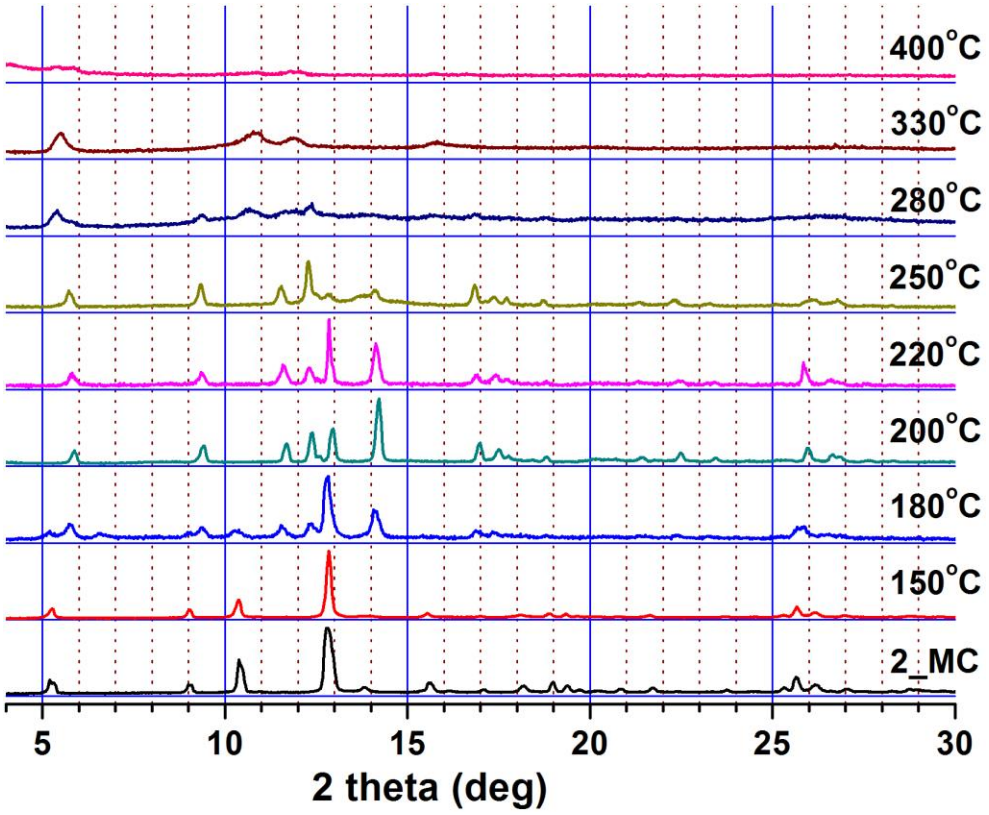

Figure 14. PXRD patterns of heat-treated **2_MC** crystals air-dried at RT heated up to 400 ºC and exposed in the air for an instance before taking the PXRD pattern.

Ligand composition of the heat-treated 2. The ligand compositions in the heat-treated samples were analyzed by using ^{1}H NMR spectroscopy. Each heat-treated sample was digested in DCl/d_6-D_2O solution (Figure S6). The ^{1}H NMR spectra were indicated that the heated crystal kept the same ratio of pz pillar to btc ligand with air-dried **2_MC** up to 150 ºC of NMR error range. Then, the ratio of pz pillar was generally declined by 0.9 pz pillar until 250 ºC, but the ratio was rapidly decreased between 250 ºC and 330 ºC as 1.6 pz pillar loss. The line graph of pz pillar integration per two btc ligands in NMR shows similar tendency of TGA of **2_MC** (Figure 15).

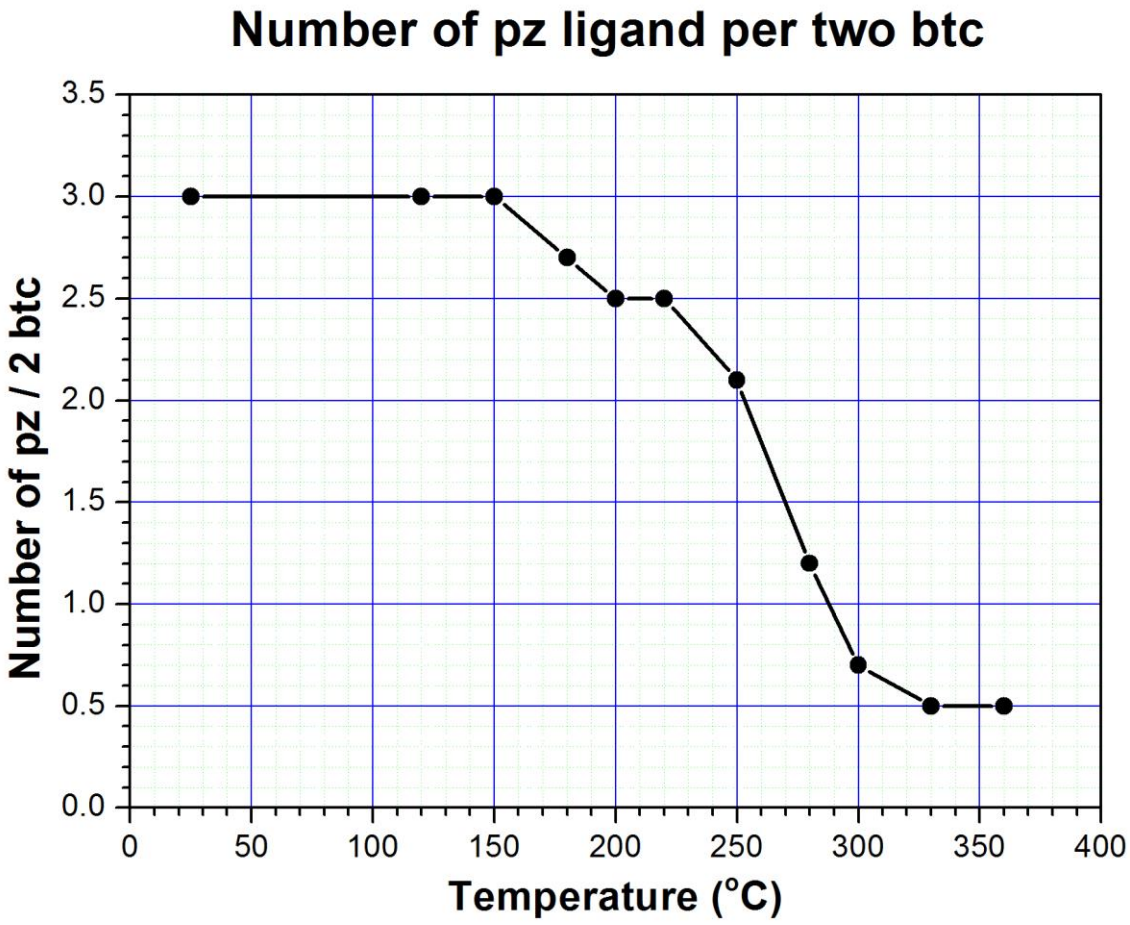

Figure 15. The line graph of pz ratios at heated **2_MC** from ^{1}H NMR spectra. (25, 120, 150, 180, 200, 220, 250, 300, 330, and 360 ºC)

Preparation of 3. Single crystals of **3** were obtained heating single crystals of **2** at 200 ºC for an hour under flowing N_2 and cooling down to ambient temperature, and then exposing the crystals in air. The EA and the ratio of btc ligand and pz pillar from the ^{1}H NMR spectrum of **3** indicate that **3** of $[Ni_6(btc)_4(pz)_{4.75}(H_2O)_6]\cdot 18H_2O$ formula unit is generated.

Crystal structure of 3. A single crystal structure analysis revealed that the lattice parameters of **3** were completely different from those of **2**. The space group of **2**, *P*2/*c*, has changed to *C*2/*m* in **3**. In the crystal structure of **3**, the approximate half of the pz pillars interconnecting mononuclear Ni2 atoms along the crystallographic *b*-axis in **2** are alternatively removed, which corresponds to one sixth of the total pz linkers in **2**. The remaining pz pillars interconnecting the mononuclear Ni2 atoms are lay down along the crystallographic *c*-axis. Each of the new Ni atoms interconnected by pz linker are further connected *via* two carboxylates of two different btc ligands as shown in the schematic drawings of Figure 17. The geometry of the other parts of the structure in **3** are slightly twisted from that of **2** but kept the same connectivity. The *trans*-coordination mode of two carboxylates in the mononuclear Ni center in **2** changed to the *cis*-coordination mode in the octahedral Ni ion of the new dinuclear Ni cluster in **3** (Figure 18). The octahedral Ni ion in the dinuclear cluster has 0.75 site occupancy and the other distorted tetrahedral Ni ion has 0.25 site occupancy. The new dinuclear Ni cluster in the crystal structure of **3** is the statistically disordered structure of the dinuclear Ni cluster of 0.25 site occupancy and of the mononuclear center of 0.50 site occupancy (Figure 19). The structure of 3 has cage-like pores at removing pz ligand positions and the largest pore dimension of **3** is 3 Å (Figure 20).

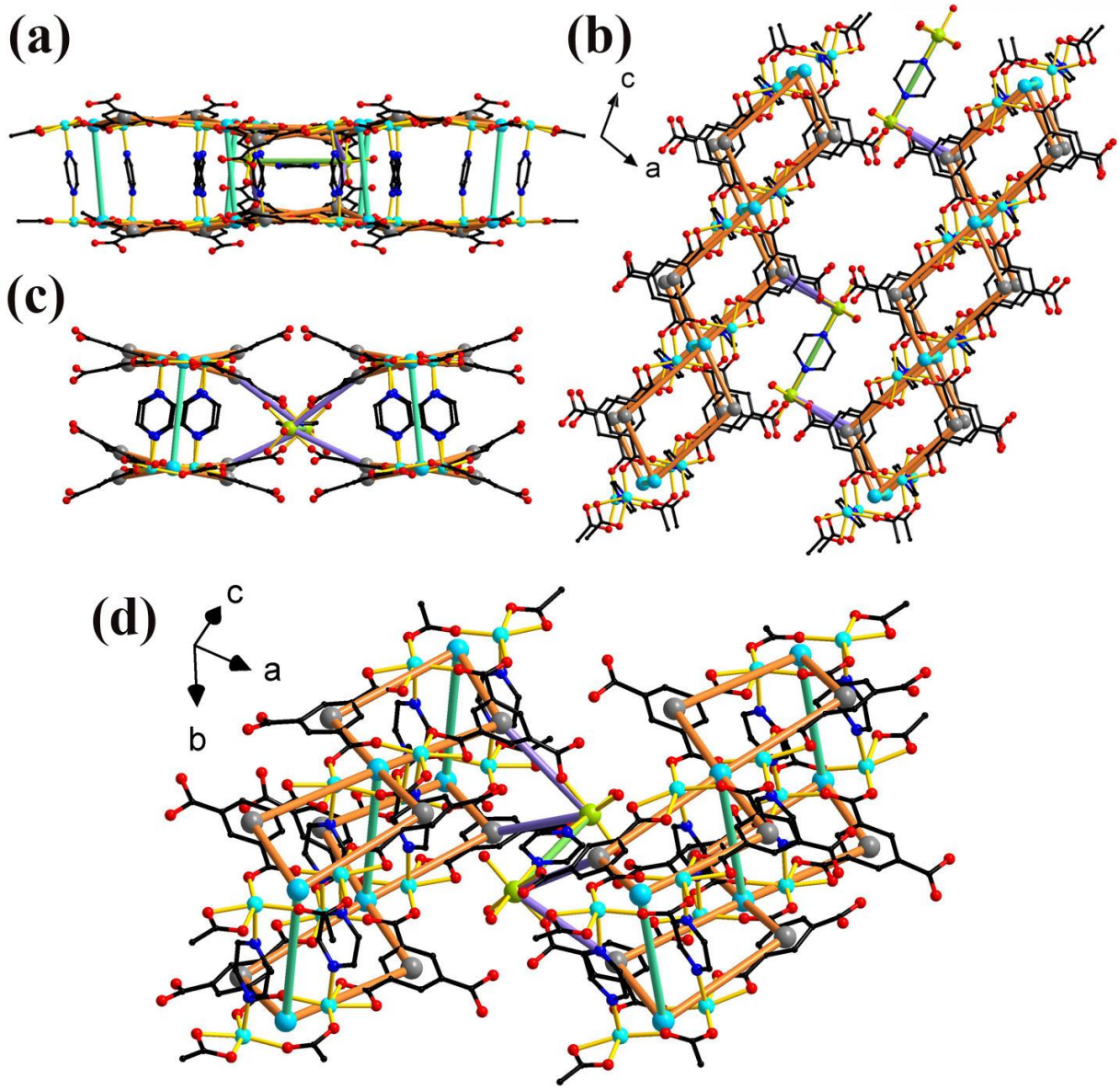

Figure 16. The crystal structure of **3**: (a) the *a*-axis view, (b) the *b*-axis view, (c) *c*-axis view, and (d) 3-P structure of **3**.

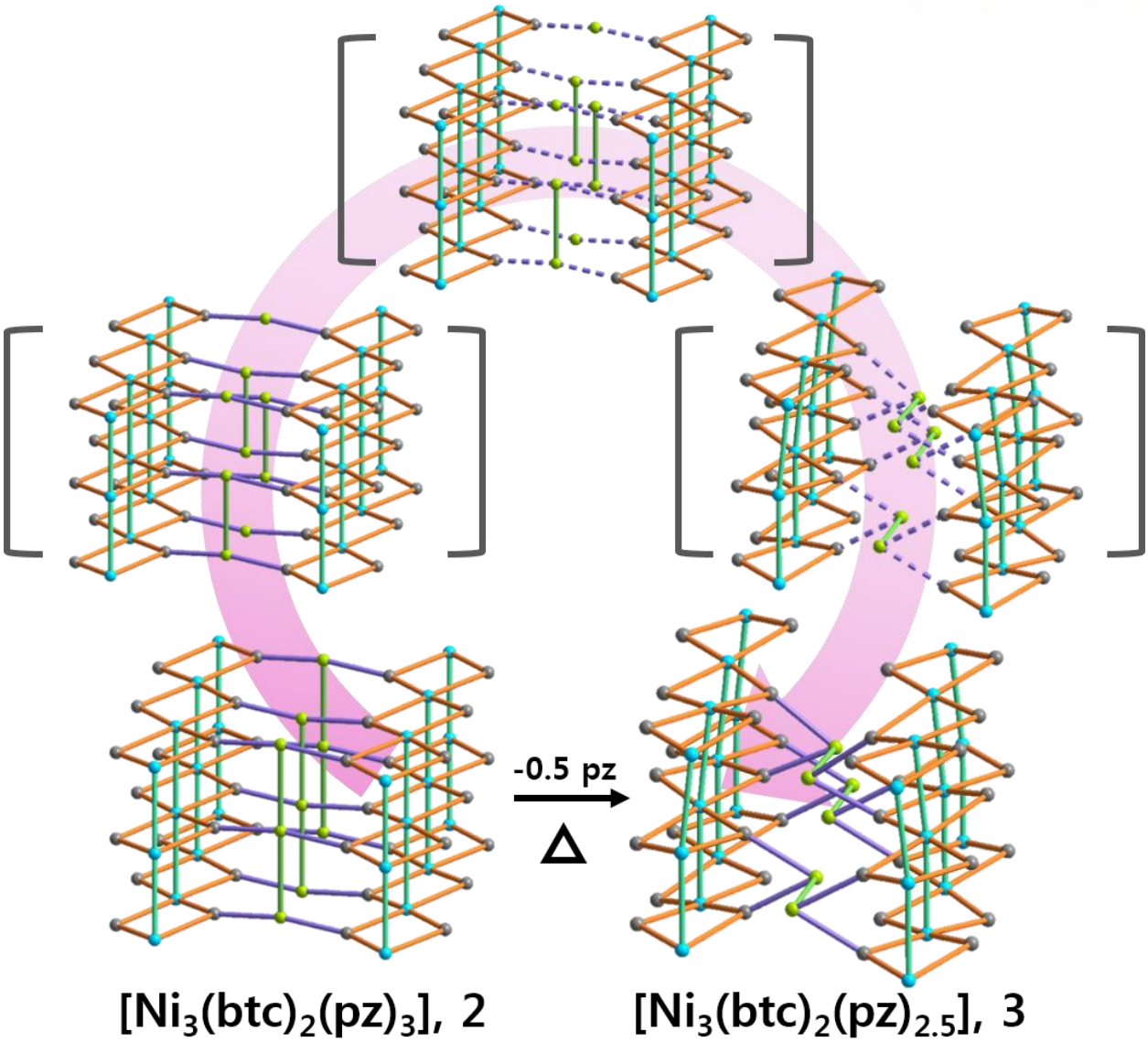

Figure 17. The expected transformation process from structure of **2** to structure of **3**.

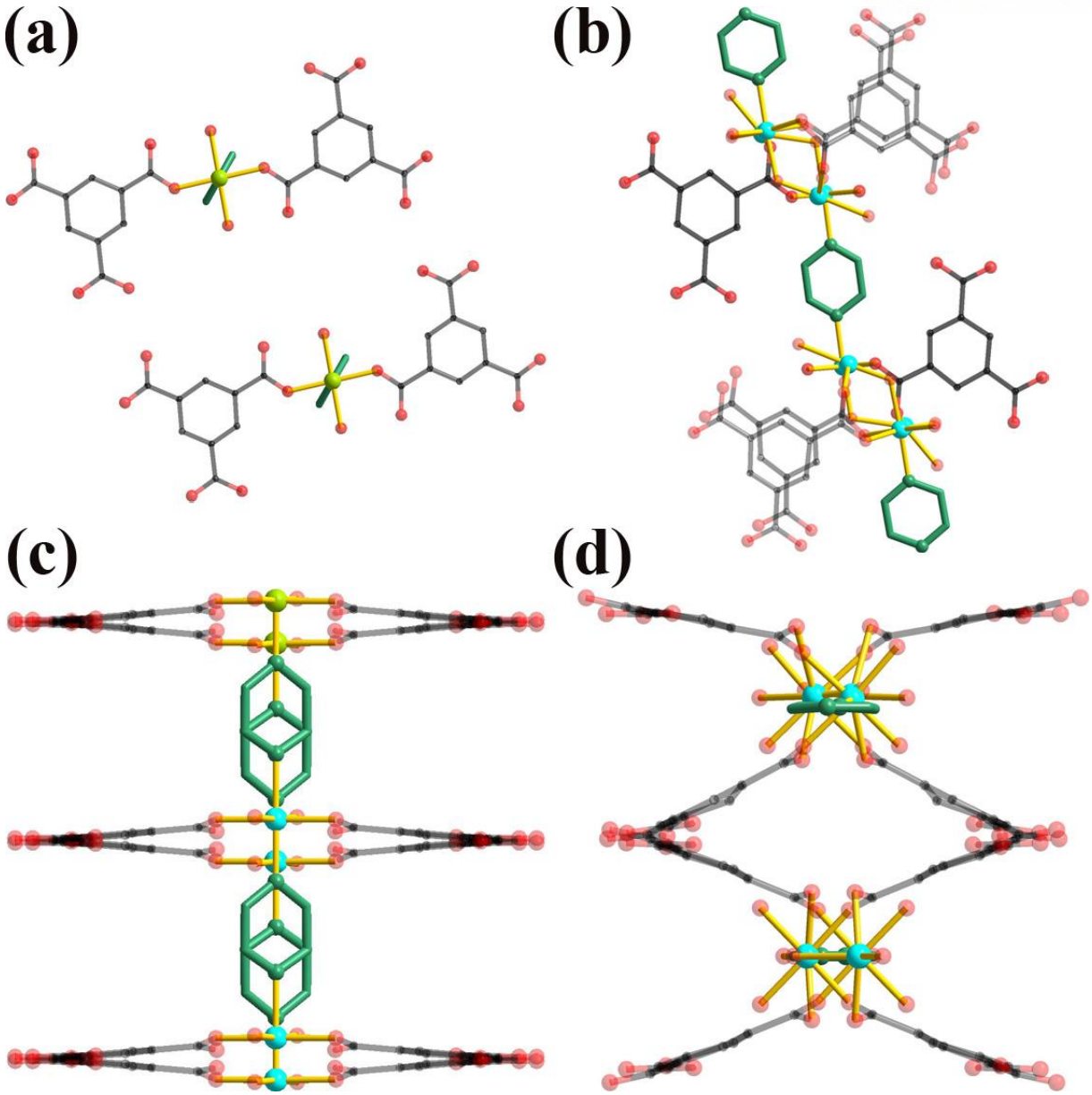

Figure 18. The detail of connection parts of layers in **2** and **3**. (a),(b) the top view of **2** and **3,** respectively. (c),(d) the *c*-axis view of **2** and **3**, respectively.

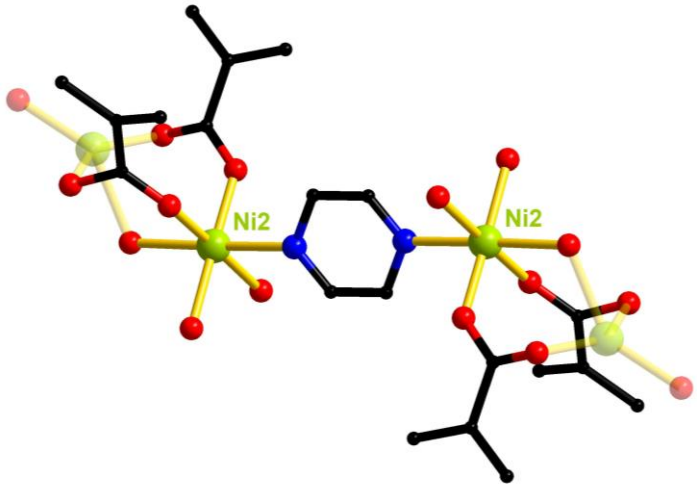

Figure 19. The new dinuclear Ni clusters interconnected by a pz linker in **3**, where the dinuclear centers are the statistical average structure of the 25% dinuclear centers and of the 50% mononuclear centers.

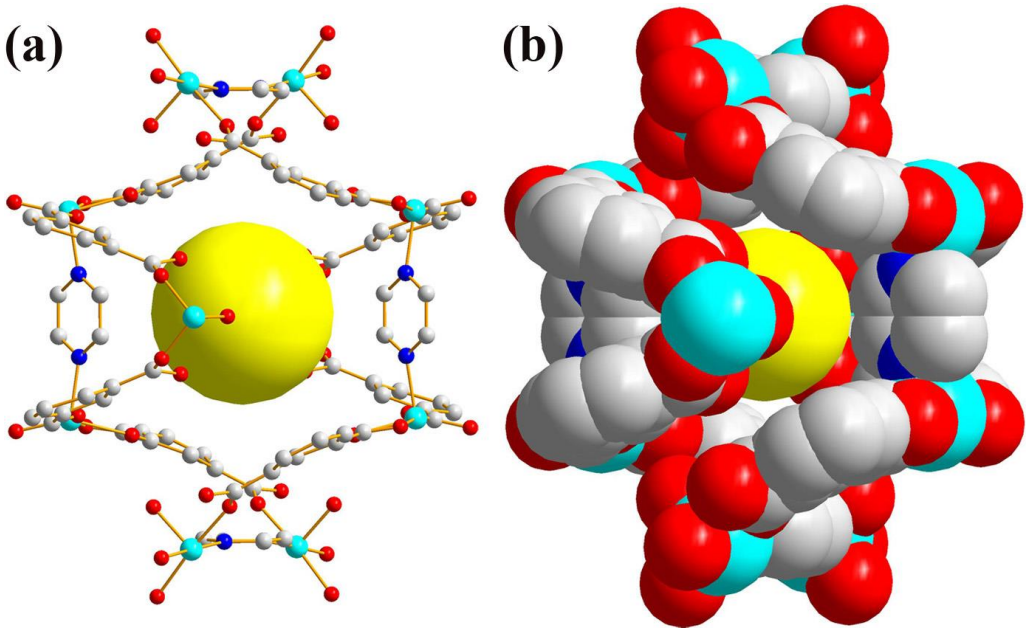

Figure 20. (a) The ball-and-stick model and (b) the space-filling model of the cage-like pore **3** with a yellow dummy ball in the center of the cavity.

3.4. Transformations of the MOFs

Transformations of the MOFs *via* ligand exchange and deletion. 1 of a 3-P 3,4,6-c **sqc130** topology that contains bipy as a pillaring ligand between the 2-P sheet of a 3,4-c **bex** topology could be transformed to the isoreticular MOF **2** with pz as a pillaring ligand (Figure 21). During the transformation from **1** to **2**, the structural rearrangement occurred in two different ways, both between the 2-P sheets of the **bex** topology and within the sheet. The first structural rearrangement is between the sheets. The intersheet distance was reduced by the pillar exchange. The second structural rearrangement is within the 2-P sheet. The interlinkage between the 1-P noded ribbons in the 2-P sheet in **1** has changed to a different interlinkage between the 1-P noded ribbons in the 2-P sheet in **2**. A set of the pairings between the two carboxylates in *trans*-binding mode in the mononuclear Ni2 center in **1** shifted to another set of the different pairings between the two different carboxylates in *trans*-binding mode in the mononuclear Ni2 center in **2**. **2** could be further transformed to **3** *via* partial deletion of the pillaring ligand pz. The controlled heating of **2** led to the systematic partial removal of the pillaring ligands and the subsequent rearrangement of the pillaring ligands.

Reverse transformations of the MOFs *via* ligand insertion and exchange. 3 can be transformed back to **2** *via* pz linker insertion (Figure 21). Simple soaking **3** in pz DMF solution at ambient condition produced **2**. The PXRD pattern of **2F3*** (***nFm**; **n** obtained from **m**) is indistinguishable from that of as-synthesized **2** (Figure 22). **2** also be transformed back to **1** *via* pillar exchange. Soaking **2** in bipy DMF solution at 100 ºC led to **1** *via* isoreticular replacement from all pz pillars to bipy pillars. The PXRD pattern of **1F2** is the same as that of as-synthesized **1** obtained *via de-novo* reaction. **3** with pz linker can also be directly transformed back to **1** *via* simultaneous bipy insertion and replacement. The PXRD pattern of **1F3** is again indistinguishable from that of as-synthesized **1**.

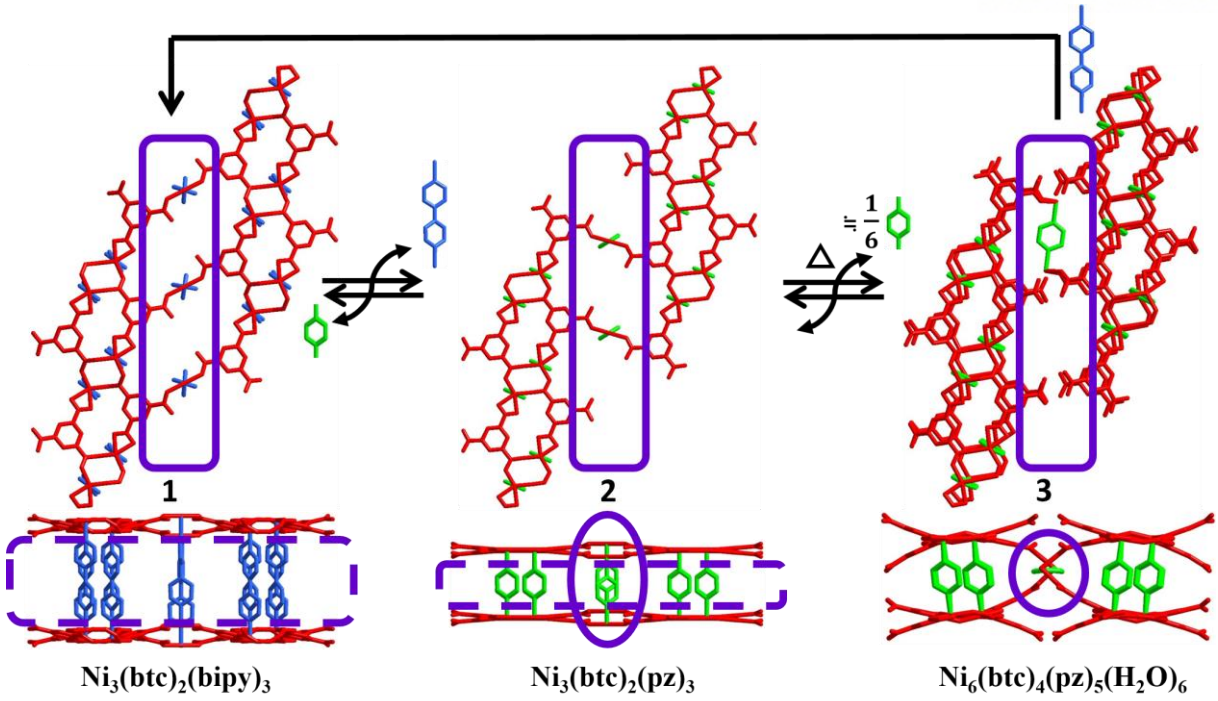

Figure 21. Scheme of single crystal to single crystal transformations.

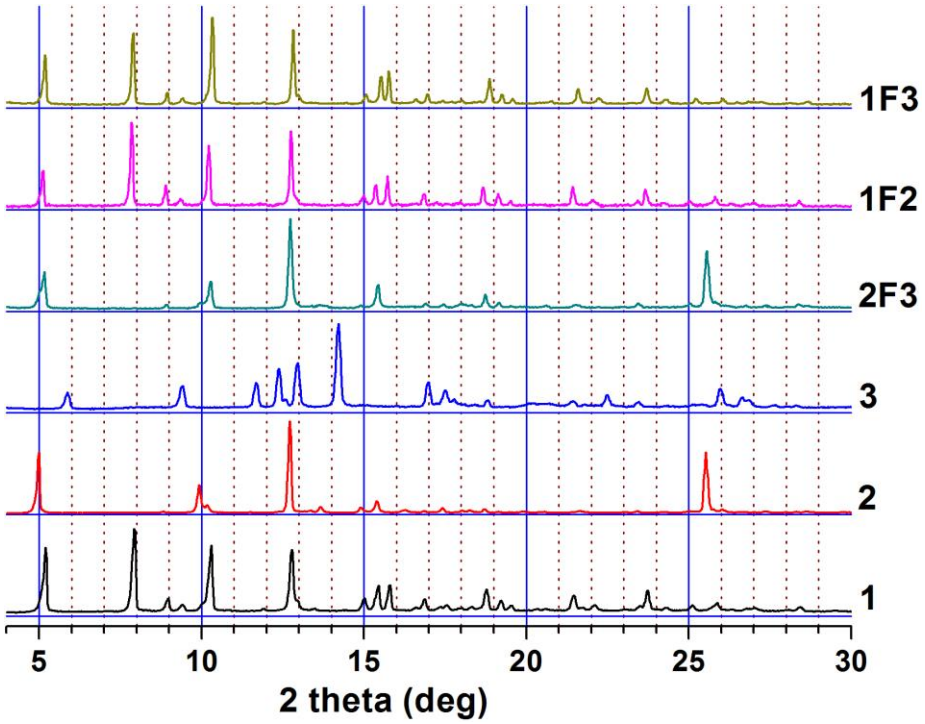

Figure 22. PXRD patterns of **1**, **2**, and **3**, and then PXRD patterns of re-transformed **2F3**, **1F2**, and **1F3**.

3.5. Sorption behaviors of the MOFs

Gas sorption behaviors of 1a. Though the PXRD pattern of activated **1a** showed the loss of its crystallinity, it still showed stepwise N_2 adsorption at 77 K (Figure 23). The very steep N_2 adsorption reaches to the first short plateau of ~ 100 cm^3/g uptake amount at ~ 0.01 P/P_0. The second uptake starts at ~ 0.02 P/P_0 and reaches to the total uptake of 399 cm^3/g at 0.96 P/P_0. While the specific pore volume of **1a** estimated from the uptake amount of 100 cm^3/g at 0.01 P/P_0 (0.155 cm^3/g) is much smaller than the calculated specific pore volume of **1** from the single crystal structure (0.459 cm^3/g), the specific pore volume of **1a** estimated from the uptake amount of 399 cm^3/g at 0.96 P/P_0, 0.617 cm^3/g, is even larger than the calculated specific pore volume of **1**. **1a** with partially collapsed pore can be restored by N_2 at 77 K. The BET surface area of partially collapsed **1a** calculated using the adsorption isotherm data of P/P_0 between 0.001 and 0.018 is 450 m^2/g. The BET surface area of the restored **1a** calculated using the adsorption isotherm data of P/P_0 between 0.048 and 0.105 is 1520 m^2/g, which is comparable to the calculated BET surface area, 1520 m^2/g, using the crystal structure model of **1**. The hysteric desorption starts at the very low pressure, ~ 0.006 P/P_0. The pore dimension of **1a** with the partially collapsed pores, 4.5 – 6.5 Å, were estimated using the isotherm data of P/P_0 up to 0.010 using NLDFT method* and that with the restored pores, 5.5 Å and 11 Å, were estimated using the isotherm data of P/P_0 between 0.048 and 0.961 using the same NLDFT method. There is no N_2 adsorption at 273 K, which is probably due to the weak interaction of N_2 with the pore surface even though **1a** has some N_2 accessible pore.

The CO_2 sorption behavior on **1a** at 195 K is similar to the N_2 sorption behavior (Figure 24). The CO_2 adsorption is also stepwise. The first steep adsorption reaches to a plateau of ~ 100 cm^3/g uptake at ~ 0.1 bar. The second adsorption step starts at ~ 0.16 bar and reaches to the total uptake of 360 cm^3/g at ~ 0.99 bar. The hysteric first desorption starts at ~ 0.1 bar and the second desorption occurs at ~ 0.018 bar. On the other hand, the CO_2 sorptions on **1a** at 273 and 298 K are far different from that at 195 K. There are no hysteresis and no stepwise adsorptions. The maximum uptakes at 273 and 298 K are 66 and 52 cm^3/g at 1.0 bar, respectively. The partially collapsed pore of **1a** was not restored by CO_2 adsorption at 273 and 298 K. The interaction between CO_2 and the framework of **1a** was not strong enough for the restoration of the partially collapsed pore. **1a** shows reversible CH_4 sorption at 195, 273 and 298 K, respectively, using its partially collapsed pore. However, the partially collapsed pore of **1a** was not restored even at 195 K by CH4 sorption.

The N_2 sorption isotherms on **2a** and **3** at 77 K are a typical type I isotherm (Figure 25). The pore volumes estimated from the maximum uptake amounts at saturation pressure, 271 and 207 cm^3/g. respectively. The BET surface areas of **2a** and **3**, 1060 m^2/g and 810 m^2/g, respectively, were calculated

using the adsorption isotherm data of P/P_0 between 0.005 and 0.031 and between 0.0001 and 0.034. The isoreticular exchange of long pillaring ligand bipy in **1a** by short pillaring ligand pz in **2a** led to the reduction of the pore volume and the surface area. The partial and systematic removal of the pz ligand in **2a** and the subsequent transformation of the framework structure to **3** further reduced the pore volume and the surface area.

The CO_2 sorption behavior on **2a** and **3** at 195 K are also similar to the corresponding N_2 sorption behaviors (Figure 26). The CO_2 sorption isotherms are typical reversible type I with no hysteresis. The maximum CO_2 uptakes on **2a** and **3** at 1 bar are 247 and 193 cm^3/g, respectively.

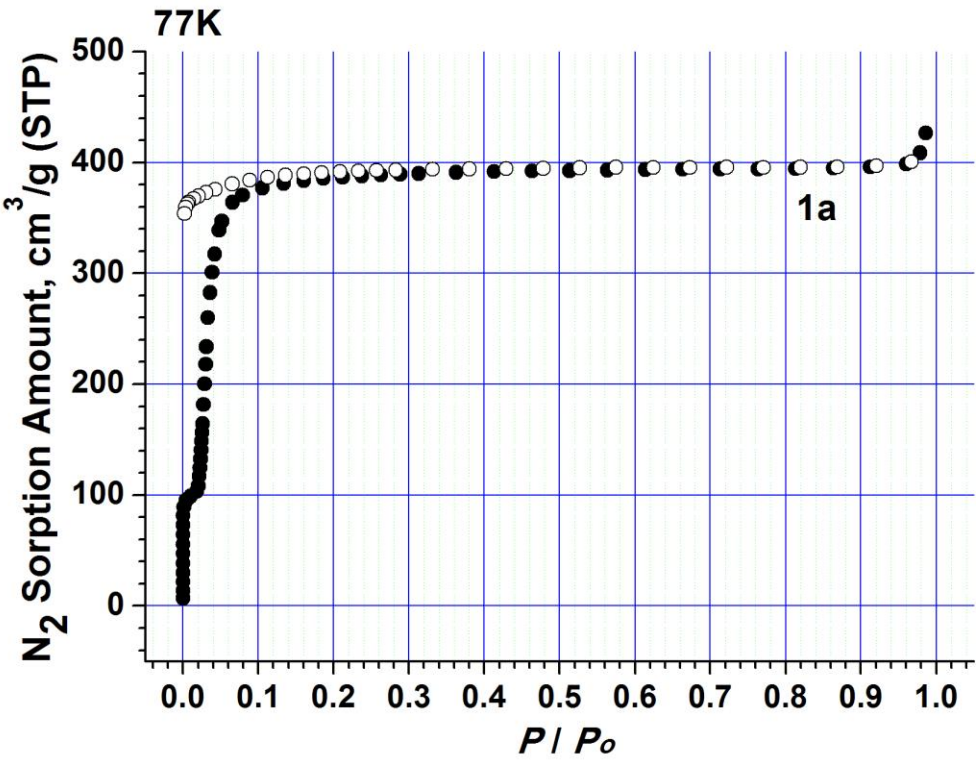

Figure 23. N_2 sorption behavior (77 K) of **1a**.

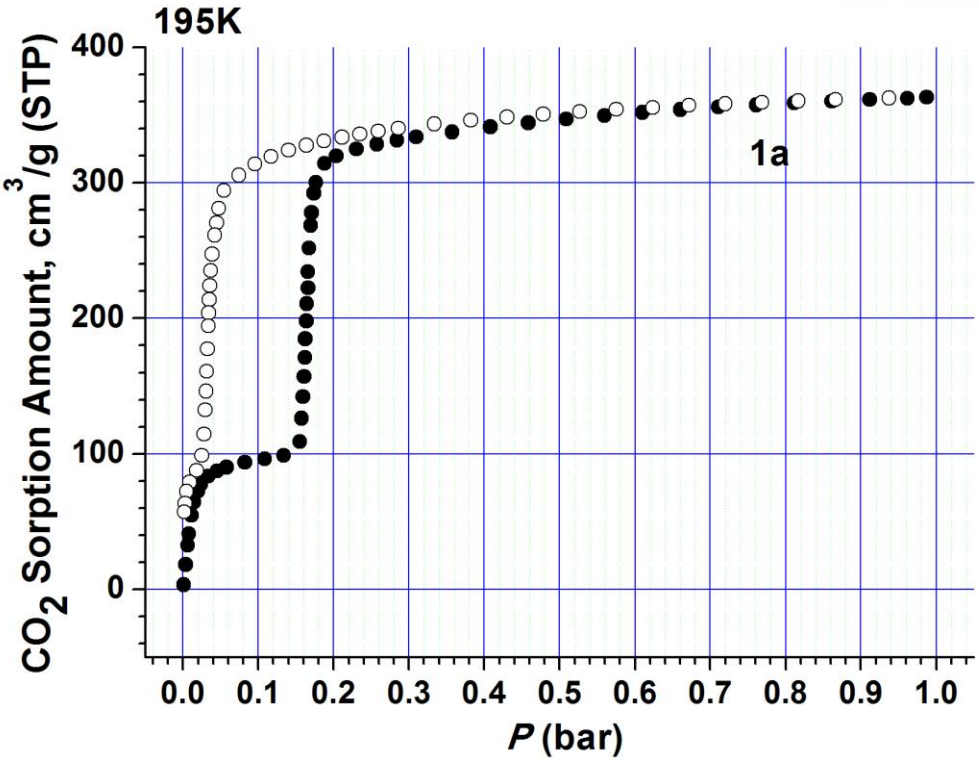

Figure 24. CO_2 sorption behavior (195 K) of **1a**.

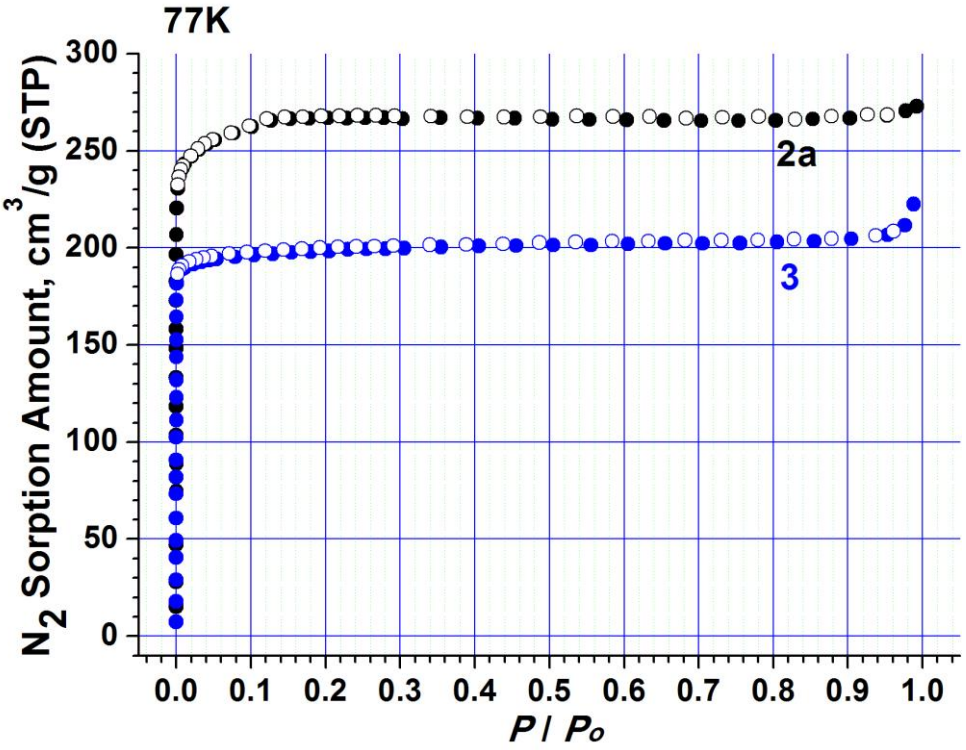

Figure 25. N_2 sorption behavior (77 K) of **2a** (black), **3** (blue).

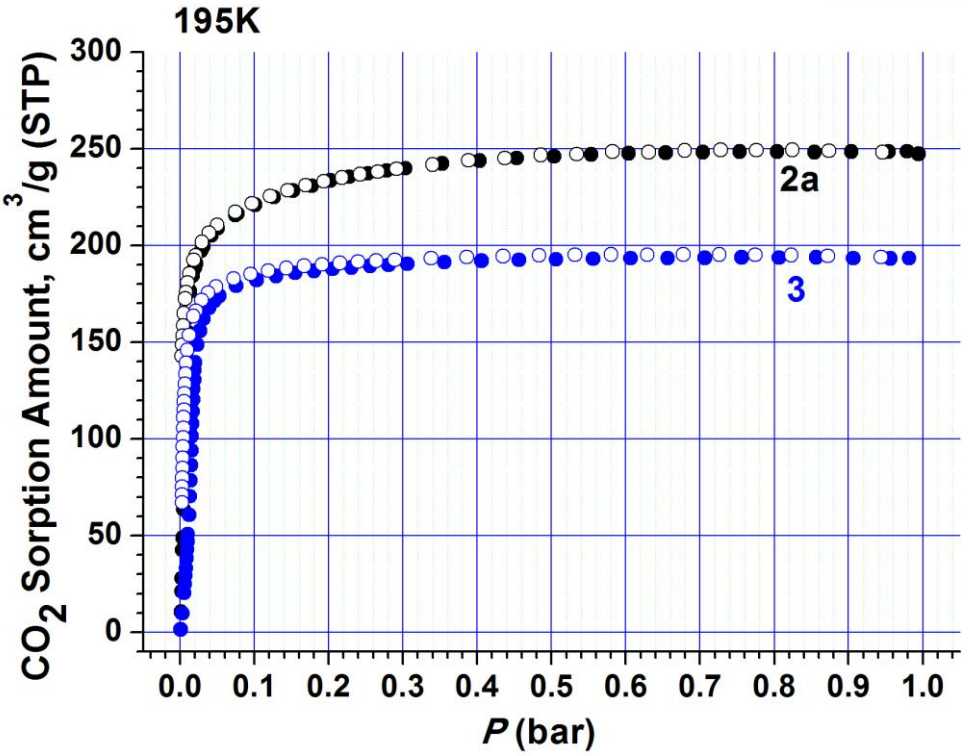

Figure 26. CO_2 sorption behavior (195 K) of **2a** (black), **3** (blue).

The CO_2 adsorption enthalpies of **1a**, **2a** and **3** were calculated using the CO_2 adsorption isotherms at 273 and 298 K, respectively (Figure 27). **1a** has the largest CO_2 adsorption enthalpy, which ranges from 36.3 to 33.5 kJ/mol (Figure 28). **1a** with partially collapsed pore can make the most effective interaction with CO_2 since it has the smallest pore dimension. The CO_2 adsorption enthalpies of **2a** and **3** range from 31.2 to 28.9 and from 20.7 to 19.5, respectively. Even though **2a** has the larger pore volume and the surface area than **3**, the pore dimension of **2a** is smaller than **3** as seen in their single crystal structures (Figure 29). The pore size analyses of **2a** and **3** from their N_2 adsorption isotherms at 77 K also support that **2a** has larger pore dimension than **1a** but has smaller pore size than **3** (Figure 30). The smaller pore dimension of **2a** than **3** is responsible for the larger CO_2 adsorption enthalpy of **2a** than **3**.

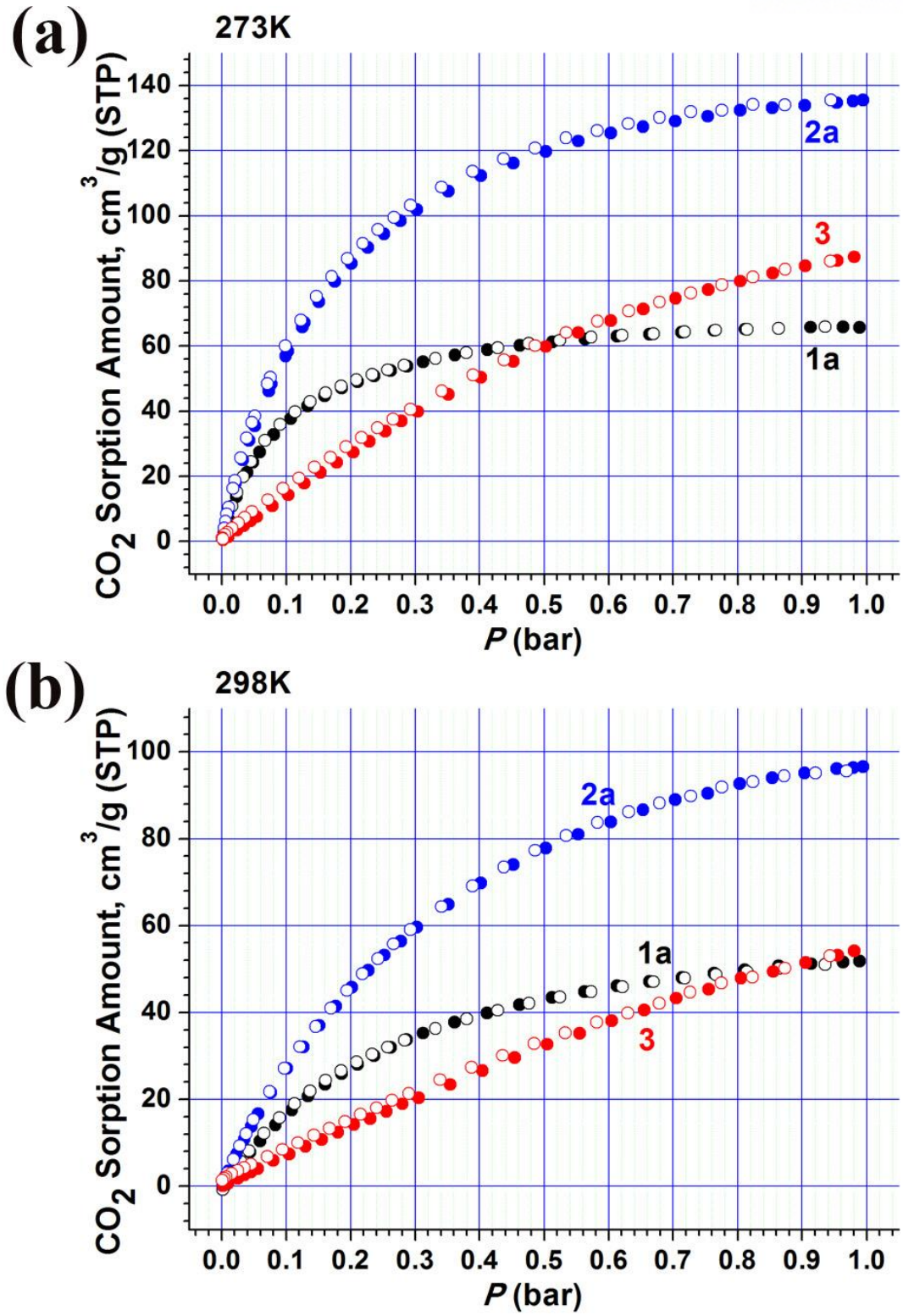

Figure 27. CO_2 sorption behavior of **1a** (black), **2a** (blue) and **3** (red) at (a) 273 K and (b) 298 K.

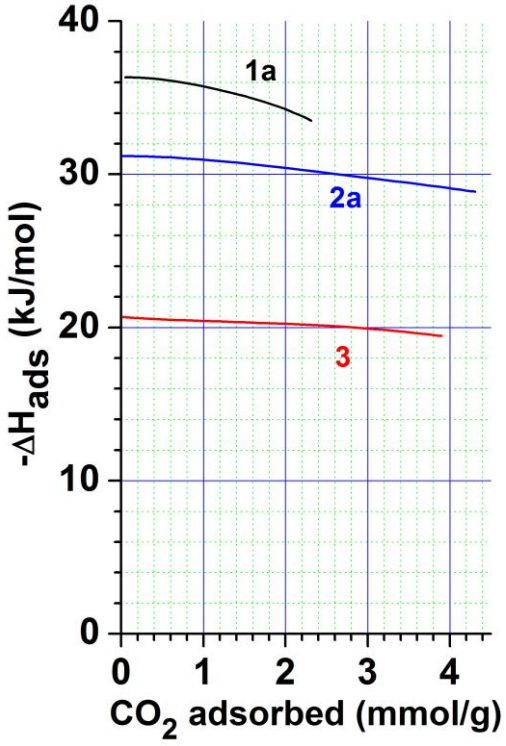

Figure 28. Adsorption enthalpy of **1a** (black), **2a** (blue) and **3** (red) by virial theory.

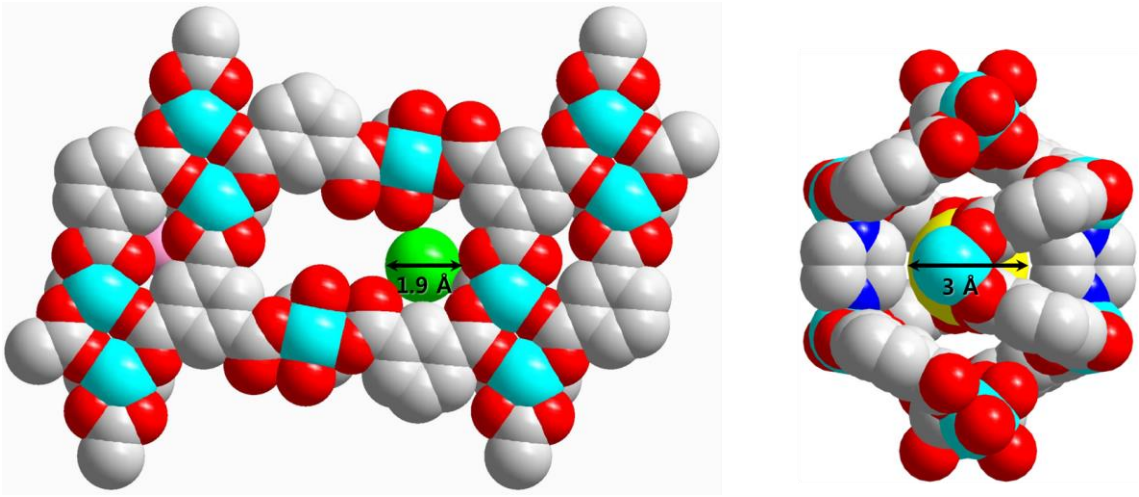

Figure 29. The space-filling models of the **2** and **3** with dummy ball . The largest diameters of pore of **2** and **3** are 1.9 Å and 3.0 Å, respectively.

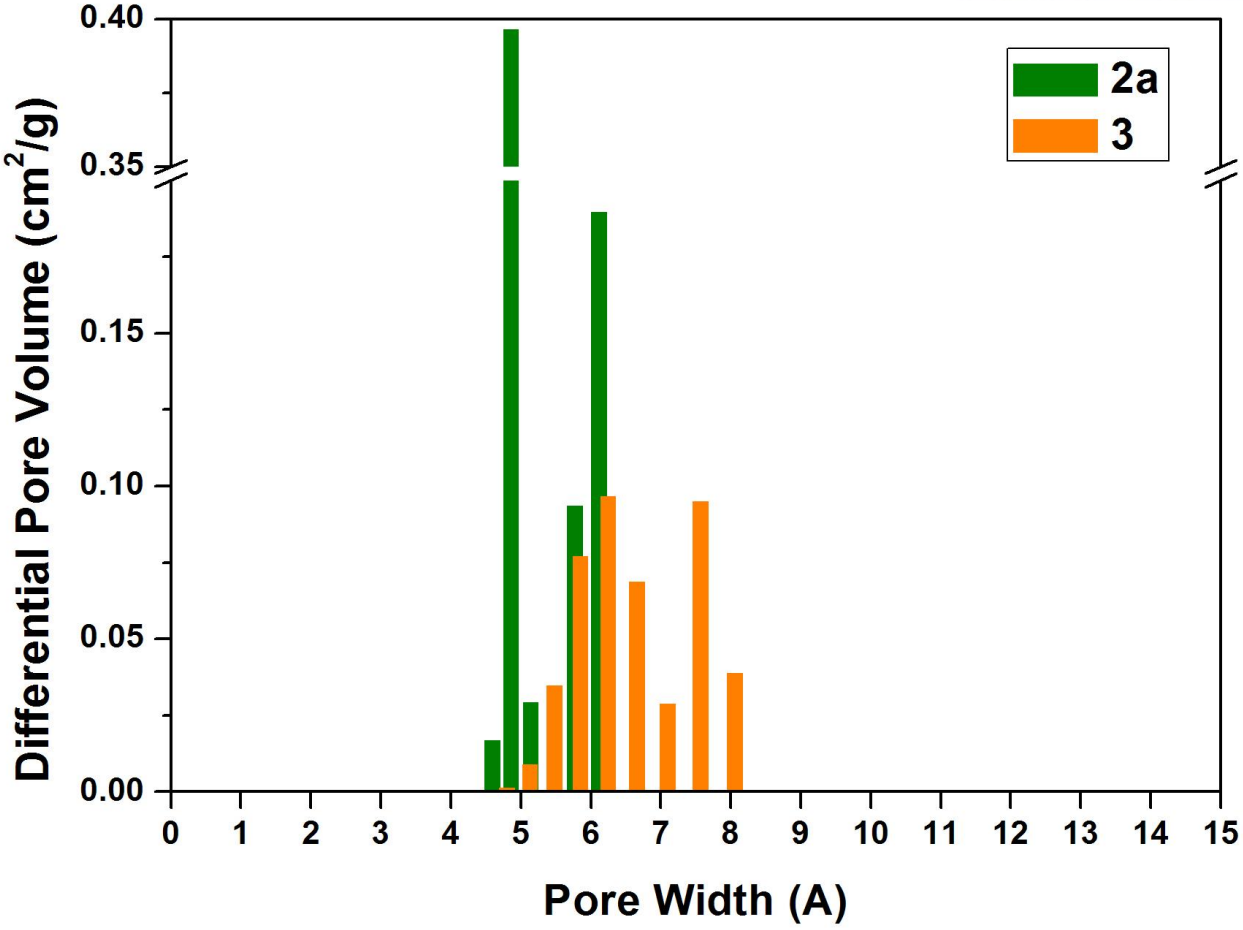

Figure 30. Pore size distribution of **2a** (green) and **3** (orange).

4. Conclusion

1 was prepared by using three different kinds of building blocks, Ni(II) ion as a potential dicationic multitopic node, btc ligand as a potential trianionic tritopic ligand and bipy as a neutral ditopic linker. The network **1** contains btc ligand as a 3-c node, a mononuclear Ni center as 4-c node, a dinuclear nickel cluster $[Ni_2(COO)_4(2N)_2]$ as a 6-c node, and bipy as a ditopic linker between the metal-based nodes. In **1**, the dinuclear nickel clusters are doubly linked *via* carboxylates of the btc ligands to form a 1-P *noded ribbon* as a supermolecular buliding block (SBB) and the SBBs are further connected to form a 3-P network by using both the mononuclear Ni centers and the two different types of bipy linkages. **1** containing 3-D solvent pores lose its crystallinity when the pore solvent molecules were removed, however, it still shows reversible N_2 and CO_2 gas sorption behaviors with significant adsorption and desorption hysteresis. The stepwise adsorptions of N_2 and CO_2 indicate the flexibility of the framework. **1** can be transformed to **2** *via* postsynthetic ligand replacement. All the ditopic bipy linkers in **1** are replaced by similar but shorter ditopic pz linkers, which leads the increase in the rigidity of **2** compared to that of **1**. The N_2 adsorption isotherm of **2** is a typical type 1 that corresponds to the sorption behavior of a rigid microporous material. The crystal structure analyses show that the transformation from **1** to **2** accompanies the first two-dimensional structural rearrangement during the postsynthetic ligand exchange. The first major structural rearrangement occurred along the neutral ditopic linker direction. The replacement from bipy to pz leads to the compressed stacking of the 2-P sheets of the **bex** topology. The second minor structural rearrangement simultaneously occurred within the sheet.

Indeed, **2** can be transformed to **3** *via* postsynthetic heat-treatment. Part of the ditopic pz linker in **2** are removed by heat-treatment. The transformation from **2** to **3** is un-expected but accompanies the rearrangement of the first three-dimensional structure by removing ditopic components of framework. In the process of transformation from **2** to **3**, 2-P layer maintained but tilted; meanwhile, big change is happened along the position of mononuclear Ni center. At mononuclear Ni center, the pz linker falls off alternatively and direction of remained pz linker is changed from parallel to perpendicular with pz pillar in 2-P layers. Besides, btc which is connected with Ni2 metal is distorted, so the bonding is broken and reformed. Above-mentioned two kinds of single crystal transformation can transform back to the original by post-synthetic ligand insertion and exchange. Also, the crystal of **3** is able to transform as **1** by both process of ligand insertion and exchange skipping the structure of **2**.

5. Supporting Information

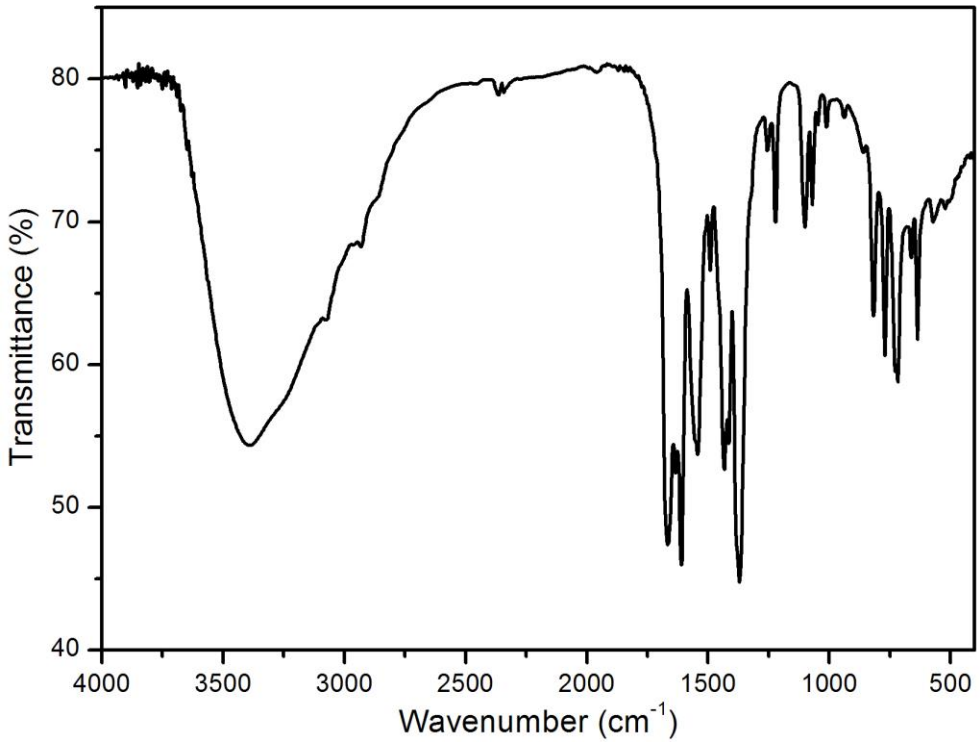

Figure S1. IR spectrum of **1**.

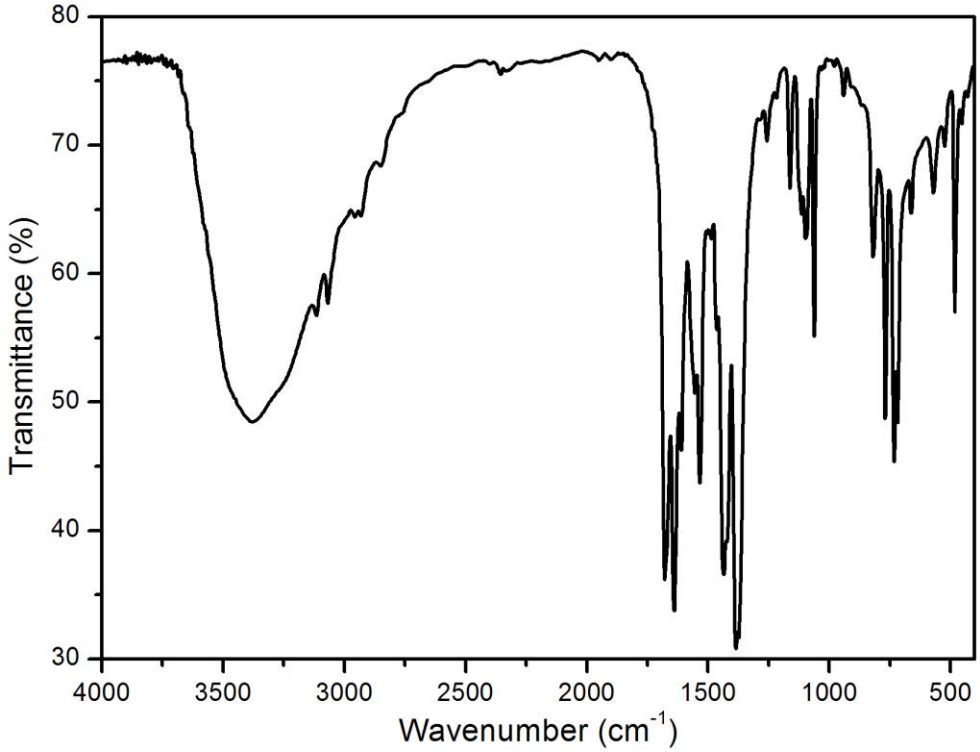

Figure S2. IR spectrum of **2**.

Figure S3. The crystal color change of **3** in air.

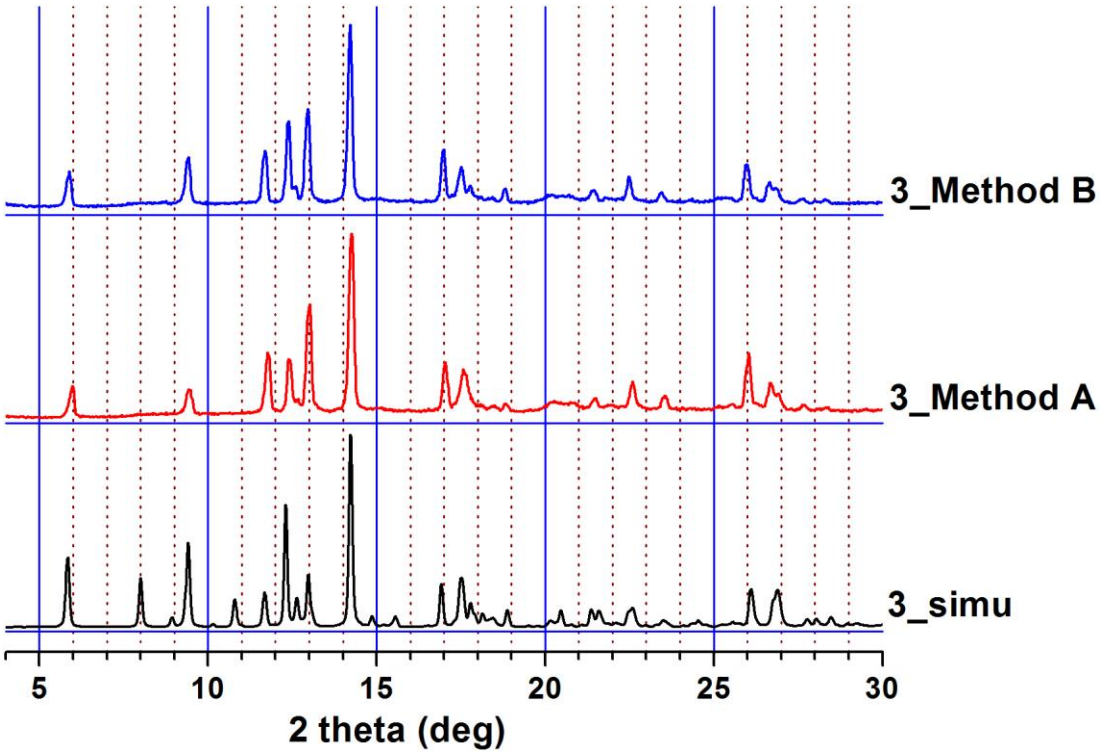

Figure S4. PXRD patterns of **3** by method A and B.

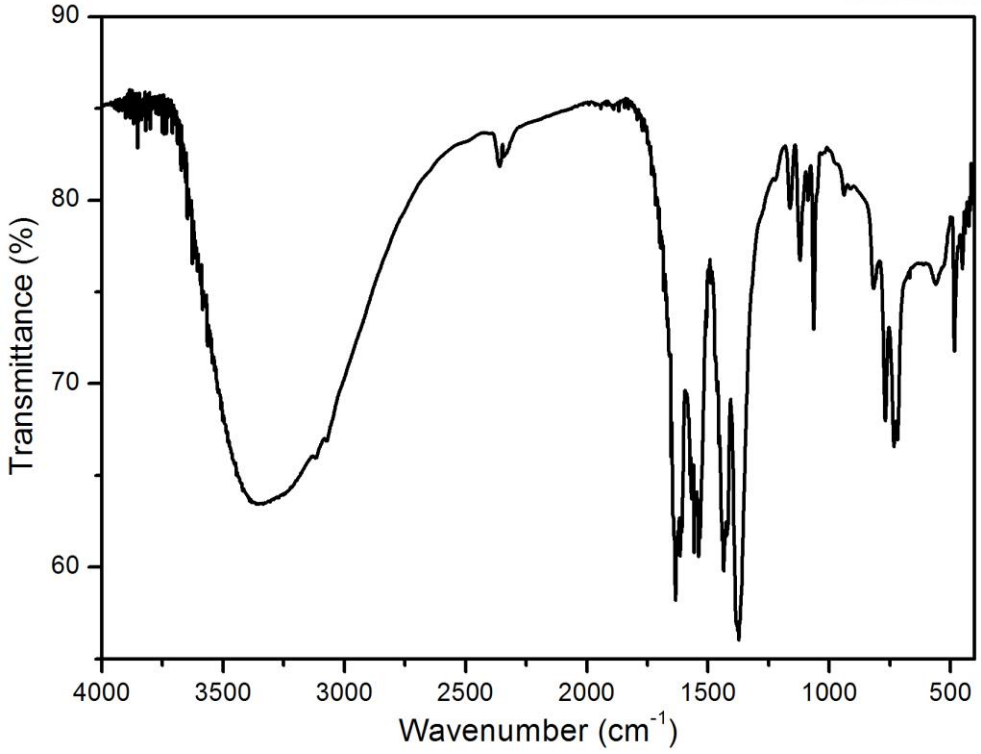

Figure S5. IR spectrum of **3**.

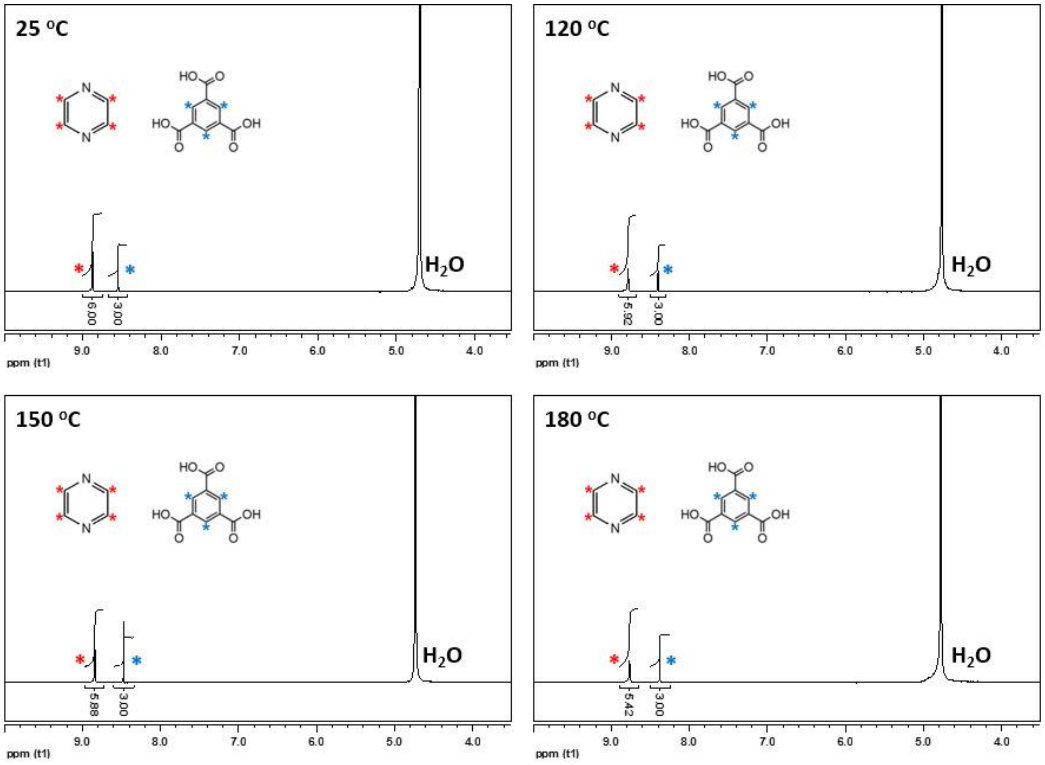

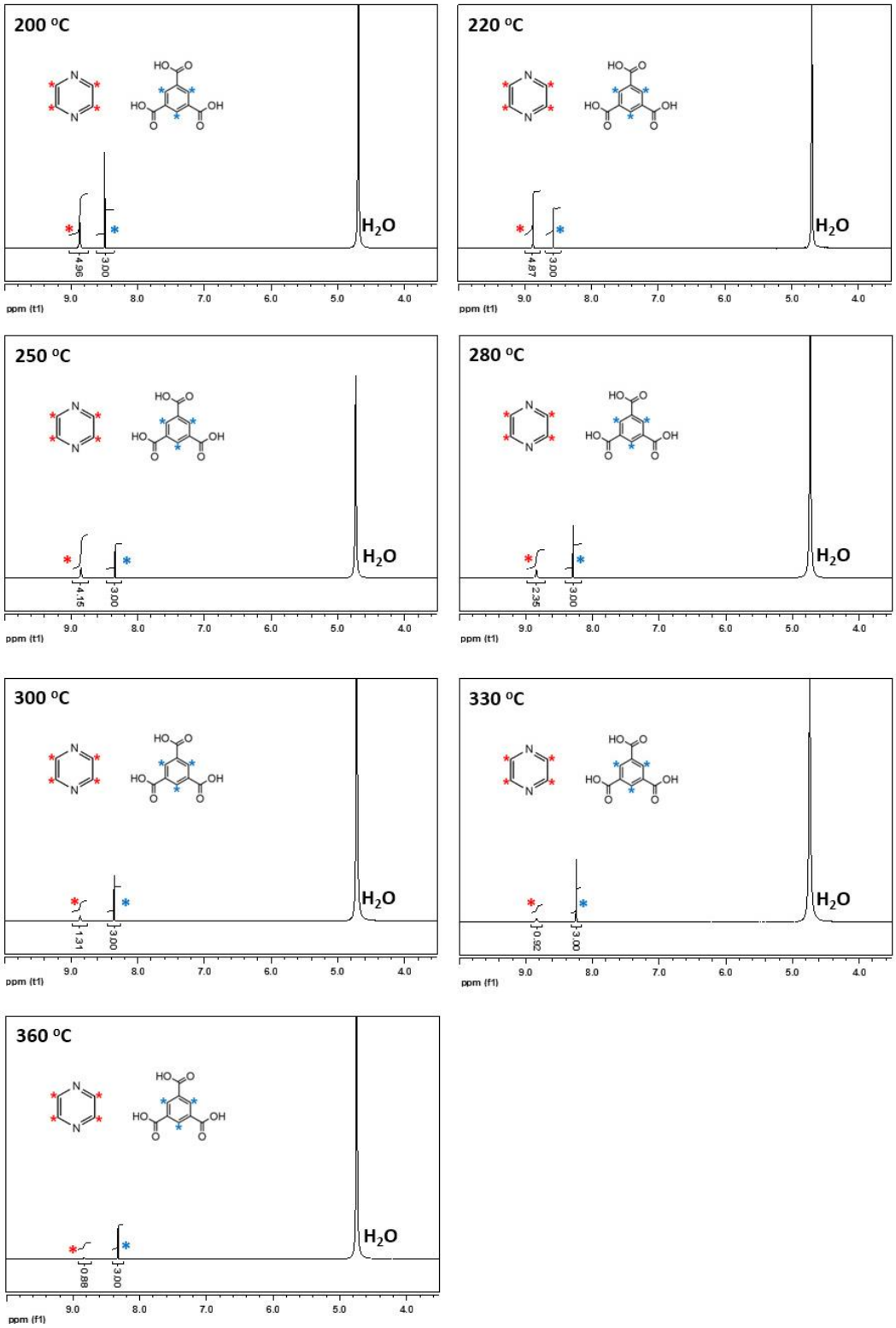

Figure S6. [1]H NMR spectra of heated **2_MC**. (25, 120, 150, 180, 200, 220, 250, 300, 330, and 360 °C)

Reference

1. (a) Zhou, H. C.; Kitagawa, S. *Chem Soc Rev* **2014**, *43*, 5415-5418; (b) Zhou, H. C.; Long, J. R.; Yaghi, O. M. *Chem Rev* **2012**, *112*, 673-674.
2. (a) Lee, Y. G.; Moon, H. R.; Cheon, Y. E.; Suh, M. P. *Angewandte Chemie* **2008**, *120*, 7855-7859; (b) Murray, L. J.; Dincă, M.; Long, J. R. *Chemical Society Reviews* **2009**, *38*, 1294-1314; (c) Horcajada, P.; Chalati, T.; Serre, C.; Gillet, B.; Sebrie, C.; Baati, T.; Eubank, J. F.; Heurtaux, D.; Clayette, P.; Kreuz, C. *Nature materials* **2010**, *9*, 172-178.
3. (a) Kaye, S. S.; Dailly, A.; Yaghi, O. M.; Long, J. R. *Journal of the American Chemical Society* **2007**, *129*, 14176-14177; (b) Horcajada, P.; Serre, C.; Vallet-Regí, M.; Sebban, M.; Taulelle, F.; Férey, G. *Angewandte chemie* **2006**, *118*, 6120-6124.
4. (a) Uemura, T.; Kitaura, R.; Ohta, Y.; Nagaoka, M.; Kitagawa, S. *Angewandte Chemie* **2006**, *118*, 4218-4222; (b) Banerjee, M.; Das, S.; Yoon, M.; Choi, H. J.; Hyun, M. H.; Park, S. M.; Seo, G.; Kim, K. *Journal of the American Chemical Society* **2009**, *131*, 7524-7525; (c) Wu, C.-D.; Hu, A.; Zhang, L.; Lin, W. *Journal of the American Chemical Society* **2005**, *127*, 8940-8941.
5. (a) Moon, H. R.; Kobayashi, N.; Suh, M. P. *Inorganic chemistry* **2006**, *45*, 8672-8676; (b) Pan, L.; Olson, D. H.; Ciemnolonski, L. R.; Heddy, R.; Li, J. *Angewandte Chemie* **2006**, *118*, 632-635; (c) Cheon, Y. E.; Park, J.; Suh, M. P. *Chemical Communications* **2009**, 5436-5438; (d) Cheon, Y. E.; Suh, M. P. *Chemical Communications* **2009**, 2296-2298; (e) Li, J.-R.; Kuppler, R. J.; Zhou, H.-C. *Chemical Society Reviews* **2009**, *38*, 1477-1504.
6. Li, J.; Huang, P.; Wu, X.-R.; Tao, J.; Huang, R.-B.; Zheng, L.-S. *Chemical Science* **2013**, *4*, 3232-3238.
7. (a) Konaka, H.; Wu, L. P.; Munakata, M.; Kuroda-Sowa, T.; Maekawa, M.; Suenaga, Y. *Inorganic chemistry* **2003**, *42*, 1928-1934; (b) Hu, C.; Englert, U. *Angewandte Chemie International Edition* **2005**, *44*, 2281-2283; (c) Ghosh, S. K.; Zhang, J. P.; Kitagawa, S. *Angewandte Chemie International Edition* **2007**, *46*, 7965-7968; (d) Mahmoudi, G.; Morsali, A. *Crystal Growth and Design* **2007**, *8*, 391-394; (e) Das, M. C.; Bharadwaj, P. K. *Journal of the American Chemical Society* **2009**, *131*, 10942-10949; (f) Li, B.; Wei, R.-J.; Tao, J.; Huang, R.-B.; Zheng, L.-S.; Zheng, Z. *Journal of the American Chemical Society* **2010**, *132*, 1558-1566.
8. (a) Haneda, T.; Kawano, M.; Kawamichi, T.; Fujita, M. *Journal of the American Chemical Society* **2008**, *130*, 1578-1579; (b) Burnett, B. J.; Barron, P. M.; Hu, C.; Choe, W. *Journal of the American Chemical Society* **2011**, *133*, 9984-9987; (c) Cohen, S. M. *Chemical reviews* **2011**, *112*, 970-1000; (d) Zhang, Z.; Zhang, L.; Wojtas, L.; Nugent, P.; Eddaoudi, M.; Zaworotko, M. J. *Journal of the American Chemical Society* **2011**, *134*, 924-927.

9. (a) Choi, S. B.; Furukawa, H.; Nam, H. J.; Jung, D. Y.; Jhon, Y. H.; Walton, A.; Book, D.; O'Keeffe, M.; Yaghi, O. M.; Kim, J. *Angewandte Chemie International Edition* **2012**, *51*, 8791-8795; (b) Kim, T. K.; Lee, K. J.; Cheon, J. Y.; Lee, J. H.; Joo, S. H.; Moon, H. R. *Journal of the American Chemical Society* **2013**, *135*, 8940-8946; (c) Gadipelli, S.; Guo, Z. *Chemistry of Materials* **2014**, *26*, 6333-6338; (d) Mukoyoshi, M.; Kobayashi, H.; Kusada, K.; Hayashi, M.; Yamada, T.; Maesato, M.; Taylor, J. M.; Kubota, Y.; Kato, K.; Takata, M. *Chemical Communications* **2015**, *51*, 12463-12466.
10. *Material Studio program*, version 3.2; Accelrys, San Diego, CA, **2005**.
11. Shin, J. W.; Eom, K.; Moon, D. *Journal of Synchrotron Radiation* **2016**, *23*, 369-373.
12. Otwinowski, Z.; Minor, W. *Methods in enzymology* **1997**, *276*, 307-326.
13. Sheldrick, G. M. *Acta Crystallographica Section C: Structural Chemistry* **2015**, *71*, 3-8.
14. Spek, A. L. *Acta Crystallographica Section C: Structural Chemistry* **2015**, *71*, 9-18.